Fault Source Models Show Slip Rates Measured across the Width of the Entire Fault Zone Best Represent the Observed Seismicity of the Pallatanga–Puna Fault, Ecuador

Nicolas Harrichhausen[*1] , Laurence Audin[1] , Stéphane Baize[2] , Kendra L. Johnson[3] , Céline Beauval[1] , Paul Jarrin[4] , Léo Marconato[1] , Frédérique Rolandone[5] , Hervé Jomard[2] , Jean-Mathieu Nocquet[4,6] , Alexandra Alvarado[7] , and Patricia A. Mothes[7]

Abstract

We explore how variation of slip rates in fault source models affect computed earthquake rates of the Pallatanga–Puna fault system in Ecuador. Determining which slip rates best represent fault-zone seismicity is vital for use in probabilistic seismic hazard assessment (PSHA). However, given the variable spatial and temporal scales slip rates are measured over, significantly different rates can be observed along the same fault. The Pallatanga–Puna fault in southern Ecuador exemplifies a fault where different slip rates have been measured using methods spanning different spatial and temporal scales, and in which historical data and paleoseismic studies provide a record of large earthquakes over a relatively long time span. We use fault source models to calculate earthquake rates using different slip rates and geometries for the Pallatanga–Puna fault, and compare the computed magnitude–frequency distributions (MFDs) to earthquake catalog MFDs from the fault zone. We show that slip rates measured across the entire width of the fault zone, either based on geodesy or long-term geomorphic offsets, produce computed MFDs that compare more favorably with the catalog data. Moreover, we show that the computed MFDs fit the earthquake catalog data best when they follow a hybrid-characteristic MFD shape. These results support hypotheses that slip rates derived from a single fault strand of a fault system do not represent seismicity produced by the entire fault zone.

Introduction

Fault-slip rates are key data used in probabilistic seismic hazard assessment (PSHA) models; however, slip-rate variability and uncertainty pose challenges in how they are incorporated in these calculations. In PSHA, seismic source characterization is the model component that accounts for the earthquake ruptures expected to impact a region of interest. A seismic source characterization may utilize both distributed seismicity sources (i.e., area sources or smoothed seismicity) and fault sources (e.g., Cornell, 1968; Youngs and Coppersmith, 1985; McGuire, 2008; Gerstenberger *et al.*, 2020). Fault sources are used to indicate higher confidence in the expected earthquake positions and geometries than the area sources, taking advantage of geological (or other) data that contribute knowledge of the fault zones' geometries and slip rates (Brune, 1968; Youngs and Coppersmith, 1985). The earthquake rates in fault source models are then constrained using fault-slip rates. There are a variety of methods used to observe fault system data, and each method may encompass different temporal and spatial scales, thus potentially resulting in inconsistent information (Styron,

1. Univ. Grenoble Alpes, Univ. Savoie Mont Blanc, CNRS, IRD, Univ. Gustave Eiffel, ISTerre, , Grenoble, France, https://orcid.org/0000-0001-8953-4292 (NH); https://orcid.org/0000-0002-4510-479X (LA); https://orcid.org/0000-0002-2614-7268 (CB); https://orcid.org/0000-0002-3789-2597 (LM); 2. BERSSIN, Institut de Radioprotection et de Sûreté Nucléaire, Fontenay-aux-Roses, France, https://orcid.org/0000-0002-7656-1790 (SB); https://orcid.org/0000-0002-3878-1215 (HJ); 3. Global Earthquake Model, Pavia, Italy, https://orcid.org/0000-0003-1369-5158 (KLJ); 4. Université Côte d'Azur, IRD, CNRS, Observatoire de la Côte d'Azur, Geoazur, Valbonne, France, https://orcid.org/0000-0001-9874-1330 (PJ); https://orcid.org/0000-0002-3436-9354 (J-MN); 5. Sorbonne Université, Institut des Sciences de la Terre Paris, ISTeP, UMR 7193, Paris, France, https://orcid.org/0000-0001-5339-4275 (FR); 6. Université Paris Cité, Institut de Physique du Globe de Paris, Paris, France; 7. Instituto Geofísico, Escuela Politécnica Nacional, Quito, Ecuador, https://orcid.org/0000-0003-4901-8175 (AA); https://orcid.org/0000-0002-0650-5531 (PAM)

*Corresponding author: n.harrichhausen@univ-grenoble-alpes.fr
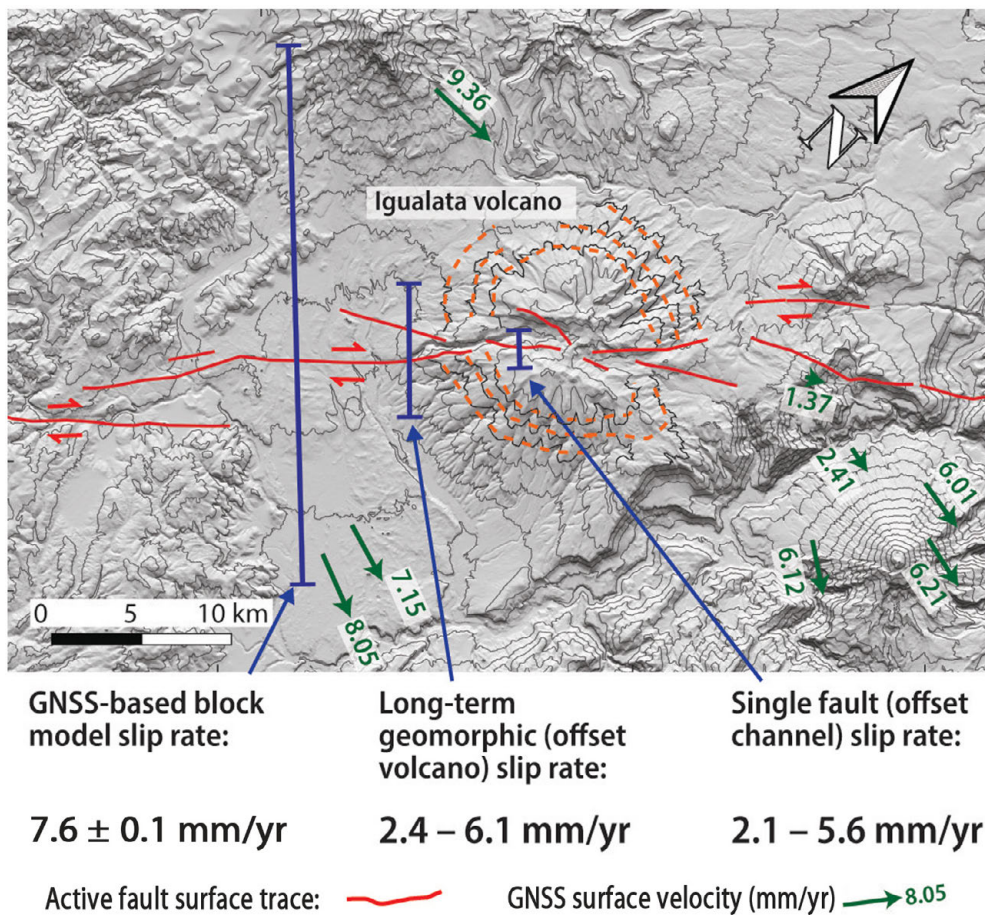
© Seismological Society of America

Figure 1. Hillshade map of the Pallatanga fault crosscutting the extinct Igualata volcano with slip rates calculated using three different methods. The geodetic block model considers Global Navigation Satellite System (GNSS) velocities with a large spacing between them (>10 km) to calculate relative motions between blocks. The long-term geomorphic slip rate uses offset contours of the Igualata volcano and considers a fault zone up ~2–5 km in width. The offset channel slip rate was measured across a single fault strand. 200 m contour spacing. Active fault segments, and geomorphic and offset channel slip rates are from Baize et al. (2020). GNSS velocities and block model slip rate are from Jarrin (2021). The color version of this figure is available only in the electronic edition.
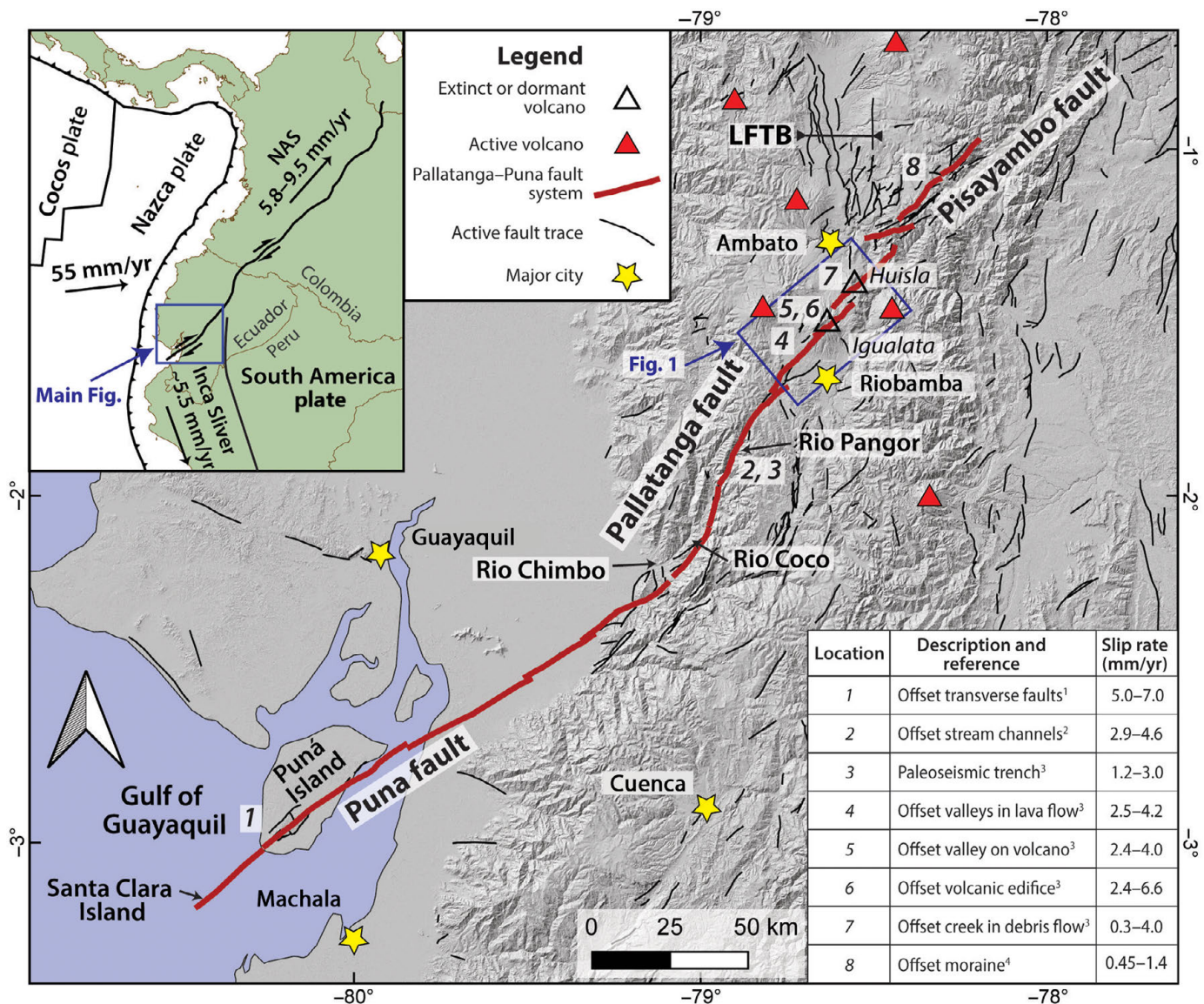
2019). This is the case for fault-slip rates in which different methods of observation, such as geodesy or paleoseismic studies, can result in conflicting rates being measured (e.g., Papanikolaou et al., 2005; Oskin et al., 2007; Baize et al., 2020). Because these data directly contribute to PSHAs in areas where there are mapped active faults, it is essential to constrain which slip-rate measurements produce earthquake rates that are most representative of the seismic potential of the fault zone.

Different methodologies for measuring slip rates can result in variable observations of the same fault due to the differences in the time frame over which they are calculated and the width of the fault zone over which they are measured (Fig. 1). The use of Global Navigation Satellite System (GNSS) surface velocities to calculate fault-slip rates is limited in time to when the earliest GNSS positions were available for a certain region, typically resulting in 10–30 yr of observations (Elliott et al., 2016), which may not represent the long-term slip rate. In addition, the width of the fault zone over which GNSS velocities are measuring deformation is constrained by the spacing of GNSS stations and is often larger (>10 km) than the width an entire fault zone. Therefore, the slip rates calculated using these widely spaced velocities may also reflect parallel faults and/or off-fault deformation (e.g., Zinke et al., 2014; Gold et al., 2015). Conversely, geological and paleoseismic methods calculate slip rates spanning over 100–100,000 yr time scales that encompass the entirety of one or several seismic cycles; however, they may be affected by temporal variability in strain rates. Individual discrete fault strands can be assessed with focused field work such as paleoseismic trenches, or entire fault zones can be studied using the offset of larger geomorphic or geologic features. An example in which the use of multiple methodologies results in different slip-rate observations occurs along the Pallatanga fault in southern Ecuador, which we investigate in this article (Figs. 1 and 2).

Slip rates have been measured along this fault using a geodetically constrained elastic block model (7.6 ± 0.1 mm/yr, Jarrin, 2021), offset of the Igualata volcanic edifice (2.4–6.1 mm/yr, Baize et al., 2020), and offset of channels and lava flows along individual fault segments (2.1–5.6 mm/yr, Baize et al., 2020). These slip rates consider a variety of time scales and different widths of the fault zone, and all differ in value and uncertainty (Fig. 1).

Which slip-rate measurements best represent the deformation contributing to the earthquake hazard of a fault zone is not well understood. For instance, observations of surface deformation during the recent surface-rupturing strike-slip earthquakes show a significant portion (up to 50%) of the total slip is observed off of the main structure (e.g., Rockwell et al., 2002; Dolan and Haravitch, 2014; Gold et al., 2015; Milliner et al., 2015, 2016; Antoine et al., 2021; Rodriguez

Figure 2. Tectonic setting and surface trace of the Pallatanga–Puna fault system (PPF). Inset in top left shows tectonic setting. Northern Andes Sliver (NAS), Inca Sliver, and Nazca plate motion (with respect to the South America plate) and boundaries are from Egbue and Kellogg (2010), Nocquet *et al.* (2014), Mora-Páez *et al.* (2019), Jarrin *et al.* (2023). Main figure shows the surface trace of the PPF and right-lateral slip rates. In addition to right-lateral slip on the PPF, the Latacunga fold-and-thrust belt (LFTB) accommodates east–west crustal shortening, and normal faults in the Gulf of Guayaquil accommodate northwest–southeast extension. Slip rates are listed in the table at bottom right, and the locations where they were measured are denoted by numbers. Citations for the slip rates are: (1) Dumont *et al.* (2005b); (2) Winter *et al.* (1993); (3) Baize *et al.* (2020); and (4) Champenois *et al.* (2017). PPF surface trace adapted from Dumont *et al.* (2005a,b), Champenois *et al.* (2017), Baize *et al.* (2020), and other active faults are from the Costa *et al.* (2020) database. Basemap hillshade derived from the Copernicus 30 m digital elevation model (DEM). The color version of this figure is available only in the electronic edition.

Padilla *et al.*, 2022). One explanation is that slip is constrained to a single structure at depth and distributed at surface, depending on the maturity of the fault zone (e.g., Dolan and Haravitch, 2014). If the majority of the slip is along a single structure at depth that distributes strain onto many faults at the surface, presumably the slip measured on one of these surface faults will underestimate the moment release during the earthquake (e.g., Dolan and Haravitch, 2014; Zinke *et al.*, 2014). Instead, the total slip rate across the entire fault zone, measured using long-term geomorphic or geodetic slip rates, would be the appropriate rate to use in a fault source model. However, comparisons of seismic moment rates with geodetic moment rates indicate that the geodetic moment rates are greater, suggesting that some deformation is aseismic and does not contribute to earthquake rates (e.g., Ward, 1998; Ojo *et al.*, 2021). Therefore, it is important to establish which slip rates best characterize the hazard from a fault system before using them in a fault source model.

The Pallatanga–Puna fault system (PPF) in southern Ecuador is one of the best studied crustal faults in South America resulting in multiple slip-rate observations (Fig. 1), a historic and paleoseismic record of large earthquakes, and consideration in regional PSHA models (e.g., Yepes et al., 2016; Beauval et al., 2018). A geodetic block model (Jarrin, 2021), geologic and geomorphic mapping (Winter et al., 1993; Dumont et al., 2005a,b; Baize et al., 2020), and paleoseismic studies (Baize et al., 2015; Champenois et al., 2017) have constrained different slip rates along the fault zone. The fault system runs close to large cities on the Ecuadorian coast (Guayaquil) and in the central Andean Valley (Riobamba and Ambato). In addition, it is thought to have hosted the most destructive earthquake recorded in Ecuador—an M 7.6 earthquake in 1797 that destroyed the city of Riobamba and killed ~25,000 people (Egred, 2004; Beauval et al., 2010). The well-documented historical earthquake record (Beauval et al., 2010) and the paleoseismic earthquake recurrence record (Baize et al., 2015) not only highlight the importance of this structure with respect to seismic hazard, but they also provide an opportunity to examine how the measured slip rates compare with longer term large earthquake frequencies.

In this article, we explore the range of possible earthquake rates permitted by the different slip rates observed on the PPF with the fault source code: Seismic Hazard and Earthquake Rate in Fault Systems (SHERIFS; Chartier et al., 2017, 2019). We use SHERIFS to model earthquake rates using slip rates and geometries of multiple segments of the PPF. We then compare the computed magnitude–frequency distributions (MFDs) from SHERIFS with catalog MFDs from a region surrounding the fault and paleoseismic records to analyze which slip rates produce MFDs that are most similar to the observed seismicity. We use SHERIFS because it allows different fault segments to rupture together or as single segments, and it allows for variation in slip rates for each fault segment, providing a realistic model of a complex fault system. It also allows the user to explore uncertainty of many variables, such as fault geometry, slip rates, ratios of on-fault to background seismicity, and the maximum magnitude (Chartier et al., 2019). Here, we establish ranges of values for these variables based on the previous publications on the PPF and the seismicity catalog, and then compare models in which slip rates, input MFD shapes, and the maximum magnitude (M_{max}) are varied.
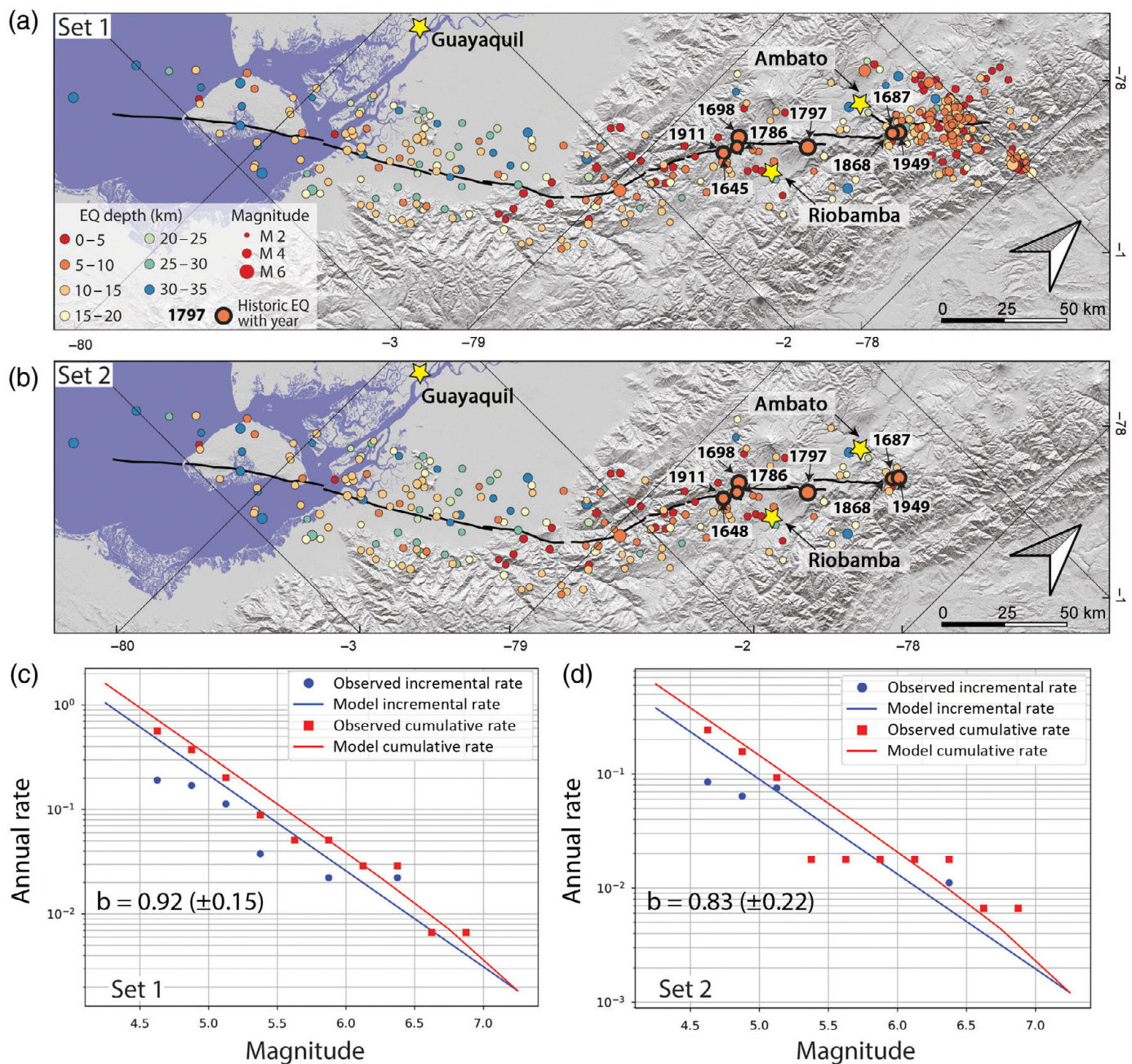
PPF

The PPF is an ~350 km long zone of active deformation in central Ecuador striking northeast from southwest of Puna Island in the Gulf of Guayaquil to the central Andes northeast of the city of Ambato (Fig. 2). This fault system represents the southernmost eastern boundary of the Northern Andean Sliver (NAS)—a continental sliver moving northeast at a rate of 5.8–9.5 mm/yr with respect to stable South America as a result of oblique subduction of the Nazca plate (Egbue and Kellogg, 2010; Nocquet

et al., 2014; Mora-Páez et al., 2019). Along this southern boundary, the PPF separates the NAS from the Inca, or Peruvian, sliver, which moves ~5.5 mm/yr southeast with respect to stable South America (Nocquet et al., 2014; Villegas-Lanza et al., 2016). Strain along the PPF is more localized than the NAS boundary to the north, where several fault branches and microblocks result in distributed deformation accommodating NAS sliver motion (e.g., Alvarado et al., 2016; Jarrin, 2021), making the PPF ideal for this study. In addition, several large historical earthquakes causing significant damage, including the 1961 M 6.3–6.8 Pepinales, 1949 M 6.8 Pelileo, 1911 M 6.1–6.3 Cajabamba, 1797 M 7.6 Riobamba, and 1698 M 7.2–7.3 Ambato earthquakes, have occurred along the northern portion of the PPF (Fig. 3a,b; Beauval et al., 2010). Paleoseismic trenching indicates that large (M > 7) earthquakes occur here every ~1000–3500 yr (location number 3, Fig. 2; Baize et al., 2015). These rich historic and paleoseismic earthquake records highlight the importance for including the PPF as a fault source in PSHA models for Ecuador (Parra et al., 2016; Beauval et al., 2018), and provides one of the best earthquake records in South America to compare fault source models with.

Oblique right-lateral relative displacement along the PPF is accommodated by a series of northeast-striking strike-slip fault segments that step northward (Fig. 2; Winter et al., 1993; Dumont et al., 2005a,b; Alvarado et al., 2016; Baize et al., 2020). At the southern end of the PPF, the Puna section of the fault system strikes northeastward toward the Andes through the actively northwest–southeast extending Gulf of Guayaquil (Dumont et al., 2005; Witt et al., 2006) and the Guayas River estuary. High levels of sedimentation have buried most of the surface trace of the fault in this region; however, right-lateral strike-slip segments have been mapped on Santa Clara Island and Puna Island (Dumont et al., 2005a,b). On south Puna Island offset transverse faults suggest 5–7 mm/yr right-lateral slip for the Upper Pleistocene across a 1 km wide fault zone (Dumont et al., 2005b).

On the Ecuadorian mainland, the Puna fault connects with the Pallatanga fault and traverses north-northwest across the Cordillera Occidental of the Andes through the Rio Chimbo, Rio Coco and Rio Pangor Valleys to the base of the extinct Igualata Volcano north of Riobamba (Fig. 2; Winter et al., 1993; Baize et al., 2015, 2020; Alvarado et al., 2016). Several overlapping fault strands have been mapped through these valleys; however, the most convincing evidence of the recent slip occurs along the Rio Pangor Valley in the Rumipamba area (Winter et al., 1993; Baize et al., 2015, 2020). Offset stream channels along the eastern slope of the valley indicate a Holocene right-lateral slip rate of 2.9–4.6 mm/yr (Winter et al., 1993). A paleoseismic trench across a fault segment on this eastern slope indicates 1.2–3.0 mm/yr of primarily right-lateral slip, during four M > 7 earthquakes with a recurrence interval of 1000–3500 yr (Baize et al., 2015).

North of Riobamaba the PPF crosscuts a volcanic avalanche deposit and Igualata, offsetting its extinct volcanic edifice

Figure 3. Instrumental–historical seismicity associated with the PPF including (a,c) and excluding (b,d) the Pisayambo fault segments. We refer to these fault segment models and catalogs as Set 1 and Set 2, respectively. (a,b) Earthquake epicenters, depths, and magnitudes; and (c,d) magnitude–frequency distributions (MFDs) and b-values for each catalog. The completeness table used to calculate b-values is shown in Table 1. Earthquakes are extracted from a 25 km buffer zone around the fault from the Beauval et al. (2013) catalog. Basemap hillshade derived from the Copernicus 30 m DEM. The color version of this figure is available only in the electronic edition.

(Fig. 1). Extensive work by Baize et al. (2020) has resulted in multiple slip rates along this portion of the fault (Fig. 2). Offset of incised valleys in the 66–32 ka avalanche deposit indicates 1.0–2.0 mm/yr and 1.0–2.7 mm/yr of right-lateral slip across two parallel fault strands for a total 2.5–4.2 mm/yr. An offset incised gully on Igualata suggests a similar 2.4–4 mm/yr of slip across a single fault strand since 60–40 ka. Offset of the Igualata edifice across an ~4-km wide fault zone indicates 2.4–6.6 mm/yr of right lateral slip since 376 ka.

Northeast of Igualata, the PPF steps northward, crosscutting the extinct Huisla volcano before stepping ~10 km northward again to several parallel northeast-striking structures including the Pisayambo fault (Fig. 2). A displaced incised creek formed in Huisla debris avalanche deposits suggest a slip

rate range between 0.3 and 4 mm/yr along a single fault strand (Baize et al., 2020). The large uncertainty in this estimation results from an incision age range from 180 to 15 ka.

Farther north along the Pisayambo fault—an offset 12–10 ka glacial moraine also suggests a lesser slip rate of 0.45–1.4 mm/yr (Champenois et al., 2017). An M 5.0 surface-rupturing earthquake in 2010 shows that this strand is active; however, nearby offset glacial deposits are indicative of parallel faults also accommodating Holocene deformation (Champenois et al., 2017).

The eastern boundary of the NAS continues northward from the Pisayambo fault toward the Cosanga fault (north of Fig. 2 map extent); however, the location and kinematics of this portion of the fault are less well constrained (Alvarado et al., 2016). In addition, where the PPF steps northward at the Igualata and Huisla volcanoes, the north–south-trending Latacunga fold-and-thrust belt branches northward, partitioning some of the strain between the NAS and stable South America (Tibaldi and Ferrari, 1992; Lavenu et al., 1995; Fiorini and Tibaldi, 2012; Alvarado et al., 2016; Baize et al., 2020). This is apparent in a geodetic-based block model of the NAS where 7.6 ± 0.1 mm/yr of right-lateral slip along the PPF decreases to 4.8 ± 0.1 mm/yr northeast of the intersection with the Latacunga fold-and-thrust belt (Jarrin, 2021). In addition to the right-lateral slip, the block model also predicts 2.2 ± 0.2 mm/yr of extension along the entire PPF. Active normal faulting is documented in the Gulf of Guayaquil (Dumont et al., 2005; Witt et al., 2006), but extension has not been observed along the Pallatanga or Pisayambo faults to the north.

Model

To compute earthquake rates produced by a segmented PPF, we use SHERIFS version 1.3 (see Data and Resources)—an open-source Python code to convert slip rates of fault segments to a moment-rate budget, which is then spent incrementally following the shape of a prescribed MFD at the scale of the whole-fault system (Chartier et al., 2017, 2019). Each fault segment's magnitude budget is spent with earthquakes randomly selected from a list of possible ruptures. This list of ruptures consists of all possible earthquakes on prescribed individual fault segments, or spanning multiple fault segments, with moment magnitudes (M) calculated using a rupture area and scaling relation (Wells and Coppersmith, 1994). Several studies suggest more appropriate scaling relations for the tectonic setting of the PPF (e.g., Hanks and Bakun, 2008; Wesnousky, 2008; Stirling et al., 2013); however, proper implementation of these different scaling relations in SHERIFS is a significant task outside the scope of this project. Possible fault ruptures are determined by setting a maximum jump distance for a rupture between fault segments, and a M_{max} that limits the maximum length of a rupture based on the magnitude-scaling relation. In addition to the magnitude budget of each fault segment, SHERIFS also uses a prediction of how much of seismicity is background versus on-fault, as a function of magnitude bins, to compute earthquake rates. It is possible for not all the magnitude budget of certain fault segments to be spent to fit the prescribed MFD shape. When a fault has a remaining moment budget, it is converted into non-main shock slip (NMS) expressed as a ratio. The detailed methodology behind SHERIFS is provided by Chartier et al. (2017, 2019).

The primary inputs for SHERIFS are fault segment geometries and a list of possible earthquake ruptures, MFD shapes defined from the seismicity catalog of the area surrounding the fault zone, a slip-rate range for each fault segment, hypotheses of the proportion of earthquakes that are on-fault versus background as a function of magnitude, b-values describing the MFD shapes, and a slip-rate sample for each fault segment. Each of these inputs defines an equally weighted logic-tree branch in our model, with the first three branches resulting in 12 independent earthquake rate models (Fig. 4a), and the last three, with a total of 90 end branches, used to explore uncertainty within each of the 12 independent models (Fig. 4b). We also expand on the 12 independent models by changing M_{max} for three of the best-fitting models. Each of these logic-tree branches are described in further details subsequently, and our input and data files for the SHERIFS models are included in the supplemental material, available to this article. Finally, to constrain which slip rates best reproduce the observed earthquake rates, we compare the absolute values of the modeled earthquake rates to the catalog MFD in each model.

Seismicity catalogs

We extracted crustal earthquake events (<35 km depth) from an area within 25 km of two fault models of the PPF from the Beauval et al. (2013) Ecuador catalog to derive MFDs for the fault system (Fig. 3). The original data set was constructed by merging eight local and international catalogs, including events between 1587 and 2009, that were homogenized to moment magnitude based on an empirical relation taken from earthquakes recorded in multiple data sets (Beauval et al., 2013). In addition, historical earthquakes (Beauval et al., 2010) with locations and magnitudes based on a macroseismic intensity database (Egred, 2009) are included (Fig. 3). Although there is significant uncertainty associated with the size and location of these historical earthquakes, their location error is relatively inconsequential, because we are computing regional MFDs for the entire fault system, and we are able to derive a more robust MFD for larger magnitudes by including them. Constraining the MFD as best as possible for larger magnitudes is essential, because we are using SHERIFS to only produce MFDs for magnitudes greater than M 4.9. The catalogs were declustered by Beauval et al. (2013) using the Reasenberg (1985) algorithm to remove aftershock and foreshock sequences, along with seismic swarms that bias the catalog to moderate and smaller magnitude earthquakes. A sensitivity study by Beauval et al. (2013) showed that varying the parameters of the declustering algorithm for the catalog had a very minor effect on the resulting Gutenberg–Richter (GR) parameters of the catalog MFD. The use of a different declustering algorithm altogether, such as
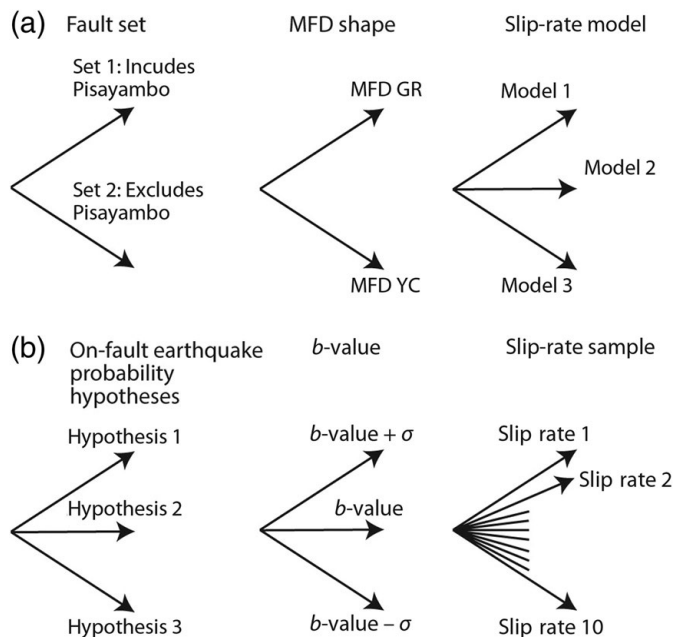
Figure 4. Logic tree for the Seismic Hazard and Earthquake Rate in Fault Systems (SHERIFS) calculations. (a) Logic-tree branches resulting in 12 independent earthquake rate models based on catalog and fault segments, MFD shape, and slip rates. (b) Equally weighted logic-tree branches within each model run based on on-fault earthquake probability hypotheses, uncertainty in *b*-values, and 10 random samples of slip rates from within the range of slip rates designated for each fault segment. The results from these 90 total end branches are plotted together on the same graph to explore uncertainty in each of the independent models described by the branches in panel (a).

the Gardner and Knopoff (1974) method, has also been shown to have a very minor impact on the earthquakes rates and subsequent hazard estimates (e.g., Beauval *et al.*, 2020). Finally, we assume time independence for the catalog and that the catalog is representative of the long term, but given that seismicity is temporally variable in nature, there is a degree of aleatoric uncertainty involved in making this assumption.

The first catalog, which we term Set 1, consists of 391 earthquakes with M 3.4–7.6 extracted from the area around the entire PPF (Set 1, Fig. 3a). The catalog consists of seven historical earthquakes, including the three largest earthquakes with M > 7 that are located close to the surface trace of the Pallatanga fault near Riobamba and Ambato. To the south along the Puna fault, earthquakes are generally smaller (M 3.4–5.2), and there are more events at depths >20 km. To the north along the Pisayambo fault, there is a seismic nest or high concentration of moderate-magnitude earthquakes that appear despite declustering (Fig. 3a). These earthquakes, which constitute >35% of the instrumental

seismicity in Ecuador (Yepes *et al.*, 2016), have been hypothesized to result from volcanic processes (Aguilar *et al.*, 1996). However, the 2010 M 5.0 right-lateral surface rupturing

earthquake on the Pisayambo fault occurred within the nest and is indicative of a seismogenic fault zone (Champenois *et al.*, 2017).

Because of the potential that some of the seismicity along the Pisayambo fault is volcanic in origin and the large quantity of moderate-magnitude earthquakes at this location, we also consider a catalog and fault model that does not include these data (Set 2, Fig. 3b). For this second catalog, we removed the Pisayambo fault segments and surrounding seismicity reducing the catalog to 228 events, which still includes the seven historical earthquakes.

We calculated GR *b*-values (Fig. 3c,d) for each of the extracted catalogs using the Weichert (1980) method in Hazard Modeler's Toolkit of the OpenQuake engine (Pagani *et al.*, 2014). These calculations are based on completeness tables, which indicates the lowest magnitude per time for which we expect the catalog to include all events that occurred. Because of the low number of events, we adapted the completeness table (Table 1) from Beauval *et al.* (2013) rather than deriving one from the catalog. This completeness table is valid for the Cordillera region of Ecuador only, whereas our extracted catalog extends along the Puna fault to the southwest away from the Cordillera. Because of this, we do not consider M < 4.5 as complete in our MFD calculations. We also do not consider earthquakes with M > 6.5 complete before 1860 due to their large uncertainties in magnitudes and locations in the historical catalog (Beauval *et al.*, 2013).

In Set 2, there are higher relative rates of large earthquakes (M ∼ 6), because we removed a large number of moderate-magnitude earthquakes (M ∼ 4) by removing the Pisayambo seismic nest. Therefore, the MFD shape of this catalog may be better described by the hybrid-characteristic earthquake model, which has a higher rate of earthquakes with a magnitude characteristic of the fault and a background of lower magnitude earthquakes with rates that decay exponentially with magnitude (Youngs and Coppersmith, 1985; Wu *et al.*, 1995), than a GR relationship where earthquake rates decay exponentially across all magnitude bins (Gutenberg and Richter, 1954). Therefore, we run SHERIFS with two alternative assumptions of the MFD: either a GR or a hybrid-characteristic (YC) distribution. Both of these distributions use the *b*-values from each catalog to describe the exponential decay of rates, and the characteristic magnitude in the YC models ranges from [$M_{max} - 0.5$] to [M_{max}], in which M_{max} is the predefined maximum magnitude of the system.

The two catalogs and the two MFD shapes result in two logic-tree branches (Fig. 4a). The first branch distinguishes between the selected fault segments with Set 1: including Pisayambo and Set 2: excluding Pisayambo. The second branch is based on whether a GR or YC distribution is used as an input into SHERIFS. Another branch of the logic tree is also based on the uncertainty of the *b*-values and is defined by the minimum, the median, and the maximum of the range of the calculated *b*-
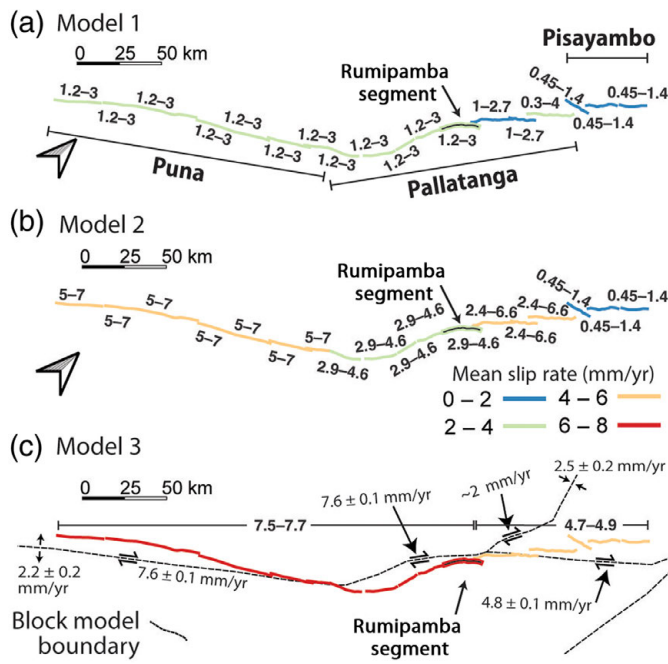
Figure 5. Slip-rate ranges (in mm/yr) and segments for each of the three slip-rate models. Slip rates used in (a) Model 1 and (b) Model 2 are derived from Figure 2, and those used in (c) Model 3 are derived from geodetic block model boundaries (Jarrin, 2021). The Rumipamba segment has a paleoseismic earthquake rate of one M > 7.0 earthquake every 1000–3500 yr (Baize et al., 2015), which we compare with the computed participation rates for this fault segment. The color version of this figure is available only in the electronic edition.

value from each catalog (Fig. 4b). This branch is one of the branches used to explore uncertainty within each of the separate SHERIFS models defined by the branches in Figure 4a.

Fault segment geometry and slip rates

We combined the mapped surface trace of the PPF system with our own surficial mapping to delineate fault segments for the two fault models (Set 1 and 2, Fig. 3a,b). Fault traces, compiled from Winter et al. (1993), Dumont et al. (2005), Alvarado (2012), Baize et al. (2015, 2020), Champenois et al. (2017), Costa et al. (2020), were used to initially delineate the main PPF (Fig. 2). We then constrained the segmentation of the PPF using a hillshaded 4 m-resolution digital elevation model, from SigTierras of the Ecuadorian Ministry of Agriculture, Quito (see Data and Resources). Segment boundaries were defined where no clear surface trace could be seen in topography, or there was a clear stepover in the fault system. These boundaries produced 18 fault segments that vary in length between ~34 and 11 km (Fig. 5).

Fault parameters including seismogenic depths, subsurface geometry, rake, and slip rate are assigned to each individual fault segment, and therefore can be varied through the fault system. For the Pallatanga and Puna segments, we use a fault

dip of 90° and a depth of 18 km to constrain the subsurface geometry. The depth is based on the lower seismogenic depth of the fault assigned by Beauval et al. (2018), which corroborates our own analyses of instrumental seismicity as a function of depth. We use a shallower depth of 12 km and a northwestward dip of 60° to constrain the geometry of the Pisayambo fault, based on fault-slip inversion using Interferometric Synthetic Aperture Radar (Champenois et al., 2017), and our own analyses of the instrumental catalog. We assigned a right-lateral slip sense with a rake of 180° to each fault segment based on the predominance of strike-slip focal mechanisms along the PPF with a nodal plane that is parallel with the fault zone (Vaca et al., 2019).

Figure 5 shows the slip-rate ranges of each PPF segment in the three slip-rate models, which correspond to the final logic-tree branch in Figure 4a. For Model 1, we use slip rates calculated across individual fault segments, such as from paleoseismic trenches or the individual fault strands that offset the Guano lava flow southwest of Igualata (Baize et al., 2020). The slip rates in Model 2 are derived from studies that consider long-term geomorphic or geologic offsets across a wider fault zone, such as the offset Igualata edifice (Fig. 1 and 2). Finally, the slip rates in Model 3 are based on the geodetic block model from Jarrin (2021). We only use the right-lateral component of slip from the block model, because we do not model dip slip. Uncertainty in slip rate is propagated through our models in SHERIFS by sampling slip rates (n = 10) uniformly from the defined ranges in each model (Fig. 4b).

SHERIFS produces a list of possible ruptures each segment participates in based on the maximum rupture jumping distance between each segment and the maximum rupture length based on a M_{max} rupture area. We selected the maximum rupture jump distance of 5 km, and a M_{max} of 7.6 to constrain the possible earthquakes. The maximum jumping distance of 5 km isolates ruptures on Pisayambo fault segments (Fig. 5) from the rest of the fault system. The rest of the PPF segments that can rupture together are limited by M_{max} of 7.6, which is the largest magnitude observed in the catalog. This magnitude also equates to the M_{max} we calculate from the instrumental catalog data using a cumulative seismic moment method (e.g., Makropoulos and Burton, 1983) in the OpenQuake Hazard Modeler's Toolkit (Pagani et al., 2014). These constraints result in 107 possible rupture scenarios with the maximum rupture length of 191 km. In our models in which the Pisayambo segments are removed, the total number of ruptures is reduced by 6 to 101. These lists of ruptures are used by SHERIFS to spend the moment budget for each fault segment, resulting in earthquake rates for the entire system for each of our models.

Paleoseismic studies and the uncertainty of the historical magnitudes suggest larger earthquakes (M_{max} = 7.9) along the PPF (Beauval et al., 2010; Baize et al., 2015); therefore, we also explore a greater M_{max} value. To do this, we do not restrict M_{max} to M 7.6 and allow the largest possible rupture (288 km) based on the

TABLE 1
Completeness Times for Magnitudes Modified from Beauval *et al.* (2013)

Magnitude	4.5–5.0	5.0–5.5	5.5–6.5	6.5–7.0
Year	1963	1957	1920	1860

length of our fault system segments, resulting in a $M_{max} = 7.8$ and 116 possible rupture combinations. In addition, to better reflect the paleoseismic and historical catalog, we increase the seismogenic depth of the Pallatanga fault to 25 km, which is deeper than the proposed seismogenic depth from Beauval *et al.* (2018), but allows for $M_{max} = 7.9$ with 114 possible rupture combinations. We use these resulting lists of ruptures in refined SHERIFS models that do not include the Pisayambo fault or a GR MFD shape, to test the effect larger M_{max} has on our final results.

On-fault earthquake probability

SHERIFS computes earthquake rates assuming some of the seismicity occurs off of the main fault. The final calculated earthquake rates are the sum of both the on-fault earthquakes and the background seismicity, which is determined by SHERIFS using a user-defined probability that earthquakes of a certain magnitude occurs on the fault plane instead of as background seismicity. These probabilities are defined for 0.5 width magnitude bins (Table 2). In our model, we use the three on-fault seismicity probability hypotheses from Chartier *et al.* (2019) in lieu of our own, because the uncertainty associated with the hypocenter locations in the Beauval *et al.* (2013) catalog and the location of the main fault plane at depth make it difficult to determine which hypocenters occur directly on the PPF. Because of these uncertainties, the hypotheses we use are arbitrary, but they cover a large spread of probabilities for M 5.0–6.5 earthquakes while restricting M >6.5 to mostly being located on the PPF. We deem this a reasonable assumption, because the probable surface rupture length for strike-slip earthquakes of this magnitude (>15–20 km, Wells and Coppersmith, 1994; Wesnousky, 2008) are more likely to be accommodated by the through-going PPF. Each of these hypotheses define a logic-tree branch within each SHERIFS model (Fig. 4b), allowing us to propagate the uncertainty associated with the different hypotheses through to our results (e.g., Chartier *et al.*, 2017, 2019, 2021).

NMS

SHERIFS spends the moment-rate budget for each fault segment iteratively until the input target MFD shape is reached, which can happen before the entire budget of a fault segment is used. This remaining moment budget is defined as the NMS and is expressed as a ratio to the slip-rate budget spent on seismogenic slip. This value can represent geologic processes, such as fault creep, or it can indicate the fault source model is not

accurately reproducing the observed seismicity if it is high (>30%–40%) (e.g., Chartier *et al.*, 2019). In our initial tests of SHERIFS, we observed that NMS ratios on segments at the end of the fault system were always higher than the rest of the system; due to the lesser number of large earthquakes these segments could be involved in compared with segments with two neighboring segments that could rupture together. We consider this an artifact of the model, and therefore we only consider the overall system NMS in comparisons of our results.

MFD comparisons

We compare cumulative MFDs from each SHERIFS model with the combined instrumental historical catalog for the fault system to determine which slip rate and MFD inputs result in a best fit with the observed seismicity. The MFDs computed in SHERIFS are represented as green density plots and a mean value of each branch in the logic tree. The range in earthquake rates represents the propagation of uncertainties in slip rates, *b*-values, and on-fault probability of the seismicity through the logic tree.

The instrumental catalog that we extracted our two catalogs from does not include uncertainties on magnitudes or locations of earthquakes (Beauval *et al.*, 2013), whereas the historical earthquakes have location and magnitude uncertainties (Beauval *et al.*, 2010). To reflect these uncertainties, we calculated 95% confidence intervals around the mean earthquake rates using the method of Weichert (1980), which is based on the number of events in magnitude bin and assumes the number of earthquake events follow a Poisson distribution about their mean. In addition, we also used different catalogs with different buffer zones around the fault system, 25 km (used for *b*-value calculation) and 5 km, for comparison with the computed SHERIFS values. We also change background seismicity zone size to reflect the geographical extent of the catalogs. The smaller buffer zones and background seismicity zones (5 km) reduce earthquake rates and increase their associated uncertainty at M < 6.0; however, comparison with these catalogs does not alter the major results of our study. Because of this lack of significant change, we only show one comparison between a 5 km SHERIFS model set and buffer zone catalog, and the rest of the 5 km buffer zone catalog comparisons are included in the supplemental material (Figs. S1 and S2b).

From their paleoseismic study south of Riobamba on the Rumipamba segment of the fault (Fig. 5), Baize *et al.* (2015) suggest that this fault segment experiences one M > 7.0 earthquake every 1000–3500 yr (Fig. 2), which we compare with our computed cumulative earthquake rates for this fault segment. The computed rates for this segment include all earthquakes that rupture it, whether or not a fault jump is involved, and are termed "participation rates" from herein (e.g., Chartier *et al.*, 2019). We plot the participation rates of the Rumipamba segment as a density plot with a mean rate and compare them with the paleoseismic earthquake rate, which is plotted as a single vertical purple bar corresponding with

the rate uncertainty. We do not plot uncertainty for paleoseismic magnitude, because the cumulative rate for M > 7 includes all magnitudes larger than this value.

Results

Figure 6 compares the computed cumulative MFDs, observed cumulative MFDs, and NMS percentages for SHERIFS Model 1–3 (individual fault strand, long-term geomorphic, and geodetic slip rates, respectively). These models either include (Set 1) or exclude (Set 2) the Pisayambo fault and surrounding seismicity, have $M_{max} = 7.6$, and use either a GR or hybrid-characteristic (YC) shape to fit the computed MFDs.

Our results show that all instances of Model 1 (individual fault strand slip rates) compute cumulative earthquake frequencies for M > 6.5 that are lower than the mean catalog rates by up an order of magnitude. However, the range in computed rates in Model 1:GR overlap with the catalog rates for M < 6.5 (Model 1: GR, Fig. 6a). The mean cumulative earthquake rates in both Set 1 and 2 versions of Model 1:YC underestimate rates for all earthquake magnitudes, and all the Model 1 results show the largest NMS ratios (29.2%–38.6%). However, the general shapes of the YC models are more similar to that of the catalog MFD.

The computed earthquake rates in Model 2 (long-term geomorphic slip rates) show a better fit with the catalog cumulative MFDs if the Pisayambo fault is removed, and they follow a hybrid-characteristic MFD shape (Set 2, YC, Fig. 6). In Set 1, Model 2:YC underestimates earthquake rates for M < 6.5 (Fig. 6a). Conversely in Set 2, the mean of the computed earthquake largely overlaps with the range of rates from the combined historic–instrumental catalog for M > 5.25, while the ranges overlap for the lesser magnitudes (Fig. 6b). For Model 2:GR in Set 1 and 2, the mean earthquake rates for M < 6.0 are overestimated, although their ranges overlap. The YC versions of Model 2 have higher NMS values (25.1% and 25.0%) than the GR models (17.2% and 16.5%).

The models using Model 3 (geodetic slip rates) have higher cumulative earthquake rates than Model 2, but show similar trends (Fig. 6). The mean rates in Model 3:GR, in both Set 1 and 2, overestimates cumulative rates for M < 5.75. In Set 1, model 3:YC the mean cumulative rates are lower than the catalog for M < 6.5, but overlap with the catalog for higher magnitudes. Finally in Set 2, the Model 3:YC mean cumulative rates largely overlap with the range in catalog rates and have a relatively low NMS value of 17.0% (Model 3:YC, Fig. 6b). Of all the models shown in Figure 6, Set 2, Model 2:YC and Model 3: YC fit best with the catalog MFD.

Figure 7 shows cumulative participation rates for the Rumipamba segment of the PPF compared with its paleoseismic earthquake rate of one M > 7 earthquake per 1000–3500 yr (Baize et al., 2015). This paleoseismic earthquake rate overlaps with the mean value of the participation rates of the Rumimpamba segment for all Set 1 models (Fig. 7a). However, only Model 1 overlaps with the paleoseismic earthquake rates in

Set 2 (Fig. 7). Model 2:YC and Model 3:YC from Set 2, which have the best overall fit when considering the entire fault system (Fig. 6), have cumulative rates for M 7.0, which are greater and do not overlap with the paleoseismic earthquake rate.

As a variation on the best-fitting Set 2 YC models, we also computed earthquake rates using $M_{max} = 7.8$ (Fig. 8a) and $M_{max} = 7.9$. Both sets of results are similar, so we only show the $M_{max} = 7.8$ results here ($M_{max} = 7.9$ is shown in Fig. S2). A larger portion of the moment budget is spent by large earthquakes in these models, so we compute greater rates for earthquakes with M > 7.5. These greater large-magnitude rates fit the catalog rates better, but cause lower rates of earthquakes with M < 7.0. This results in the mean rates for all models being lower compared with the mean catalog rates across most magnitude bins. The spread of rates in Model 3, however, overlaps with the range in rates in the catalog for most magnitudes and again has the best fit with the observed rates. Model 3 also has the smallest NMS value of 13.8%.

In addition to testing a larger M_{max}, we also compare these models with observed rates computed from a catalog extracted from a 5 km buffer zone around the PPF (Fig. 8b). This much smaller catalog still includes most of the larger earthquakes, but has lower catalog rates for M < 7.0. Despite this change, Model 1 still underestimates earthquake rates across most magnitude bins. Models 2 and 3 fit better for M < 7.0 with the mean computed rate overlapping with the 95% confidence interval of the observed rates across all magnitudes.

Finally, we show the participation rates for the Rumipamba segment for the $M_{max} = 7.8$ models (Fig. 8b). Similar to the $M_{max} = 7.6$ models (Fig. 7), only the mean cumulative participation rate of Model 1 overlaps with the paleoseismic earthquake rate from Baize et al. (2015). The range of computed participation rates for Model 2 also overlaps with the paleoseismic earthquake rates, whereas there is no overlap between the paleoseismic earthquake rates and Model 3.

Discussion

Our initial results show that the computed earthquake rates from Model 2:YC and Model 3:YC in Set 2, irregardless of M_{max}, have the best fit with the catalog earthquake rates of the PPF (Fig. 6). This result suggests the following two implications: First, slower slip rates derived from studies on single fault strands (Model 1) do not provide enough of a moment budget to reproduce the observed seismicity of the fault system while maintaining the prescribed MFD shapes. Conversely, the faster geodetic and long-term geomorphic slip rates (Model 3 and Model 2) better reproduce the observed seismicity and should be weighted more heavily in a fault source model of the PPF. This result also holds when comparing the computed rates with catalog rates from within only 5 km of the fault zone. Second, the inclusion (Set 1) or exclusion (Set 2) of Pisayambo seismic nest has a significant impact on the MFD shape derived from the catalog and used to constrain that

TABLE 2
Hypotheses of Probability That a Given Earthquake Occurs on the Pallatanga–Puna Fault System (PPF) Instead of as Background Seismicity, as a Function of Magnitude

Magnitude	4.9–5.0	5.0–5.5	5.5–6.0	6.0–6.5	6.5–7.0	7.0–7.5	7.5–8.0	8.0
Hypothesis 1	0.1	0.1	0.1	0.4	0.6	0.75	0.95	0.999
Hypothesis 2	0.2	0.4	0.5	0.7	0.7	0.85	0.999	0.999
Hypothesis 3	0.2	0.5	0.6	0.75	0.8	0.9	0.999	0.999

of the fault system; when it is excluded, the combined historic and instrumental catalog best follows a hybrid-characteristic earthquake model (e.g., Youngs and Coppersmith, 1985).

The result that the iterations of Model 1 do not reproduce and largely underestimate the observed seismicity supports the hypotheses that slip rates measured across single surface strands are not representative of the entire fault system (e.g., Dolan and Haravitch, 2014; Zinke et al., 2014). This may be especially relevant in regions of higher fault complexity such as fault bends, because surface strain may be more distributed across many structures at shallow depths compared with a less segmented and straighter portion of the fault (e.g., Visage et al., 2023). Measuring a slip rate across a single one of these structures in a distributed fault zone would miss slip on parallel fault strands (e.g., 2016 Kaikoura earthquake, Hamling et al., 2017; Williams et al., 2018) or off-fault deformation (e.g., 2019 Ridgecrest earthquake, Antoine et al., 2021; Rodriguez Padilla et al., 2022). Much of the PPF is characterized by left-stepping restraining bends or stepovers north of a latitude of −2.5°, and this is where all the slip rates used in Model 1 were measured (Fig. 2). Thus for the PPF, the faster geodetic or long-term geomorphic rates used in Model 2 and 3, and measured across the entire fault zone (Fig. 1), better estimate the fault system seismicity. These slip rates encompass the strain accumulation of the whole system, and they probably are more representative of the slip rate at depth, where the fault system narrows and large earthquakes tend to nucleate (e.g., Meissner and Strehlau, 1982; Sibson, 1982; Das and Scholz, 1983; McNulty, 1995; Dolan and Haravitch, 2014). Despite this conclusion, care still must be taken when using geodetic and long-term geomorphic slip rates due to the limited temporal scale the geodetic rates cover (<30 yr) or the long-time intervals the geomorphic and geologic offsets may cover (≫ 10 ka), which can miss temporal slip-rate variability. Therefore, if possible, as many types of slip-rate measurements as possible should be used and compared in fault source models.

The exclusion of the Pisayambo seismic nest (Set 2) changes the shape of the observed MFD of the PPF, impacting which SHERIFS model produces an MFD that fits best with the catalog rates. When the abundant moderate-magnitude (M 4.0–5.5) earthquakes in the nest are included in the MFD, the distribution of rates for M < 6.0 resembles a GR distribution (Fig 3). In this case the Set 1, Model 1:GR MFD fits well with M < 6.0 earthquakes but underestimates the large earthquake frequencies (Fig. 6a). Because most of the large (M > 6.5) earthquakes are located away from the Pisayambo fault (Fig. 3), this fit with lower magnitudes may suggest that Set 1, Model 1:GR may work best in computing seismicity for only the Pisayambo segments. If this seismicity nest is a phenomenon that occurs along the entire PPF, then it would be important to use it in the analysis of the whole system. However, because the nest has been attributed to local volcanic processes (Aguilar et al., 1996), the computed MFD for the entire PPF should not be compared with the seismic nest. Instead, we advise the Pisayambo fault segments be modeled separately from the rest of the PPF using different inputs derived from a MFD of the seismic nest.
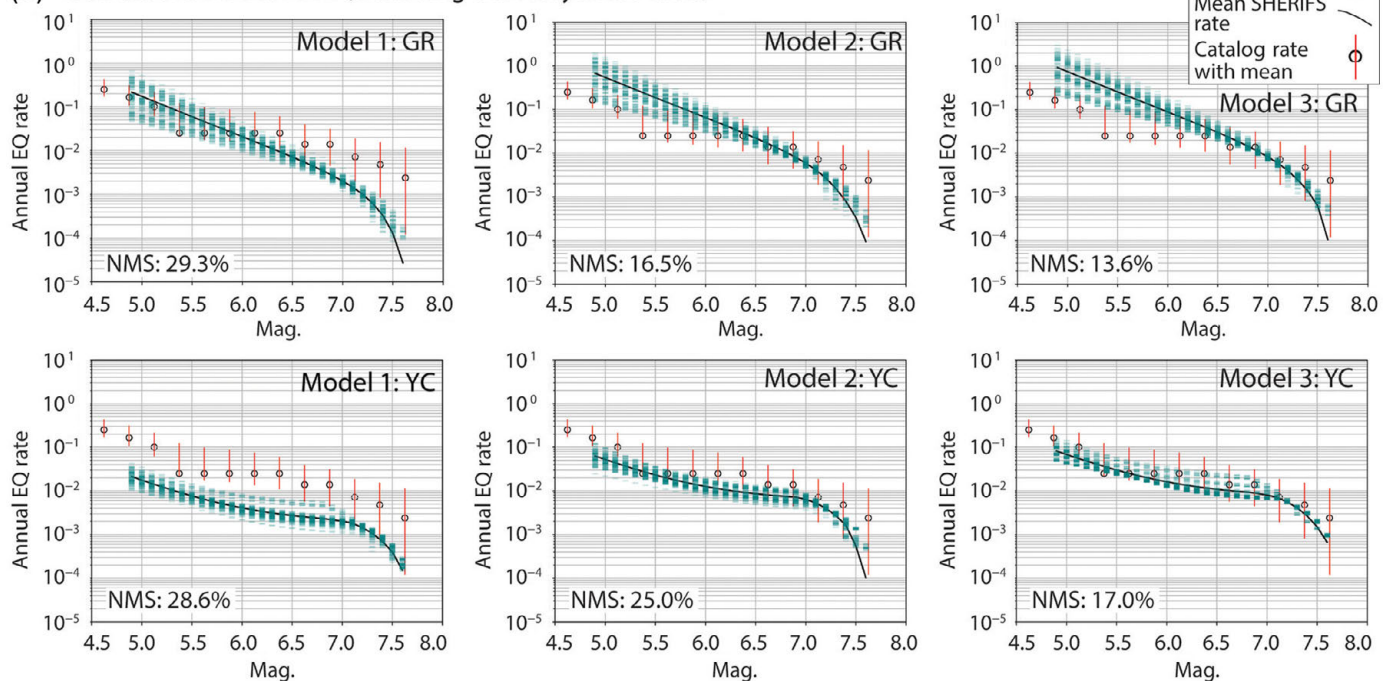
In addition to changing the shape of the catalog MFD (Fig. 3), removing the Pisayambo fault and related seismicity removes a section of the fault system where we expect there is more distributed deformation. The low slip rate (0.45–1.4 mm/yr) along the Pisayambo fault may be indicative that strain is being accommodated on parallel fault strands. To the northeast of the Huisla volcano, several fault strands may branch away from the main structure resembling a horsetail typical of the end of a fault system (Fig. 2). Also, the Latacunga fold-and-thrust belt to the east is known to be accommodating horizontal shortening at this location (Fig. 2; Tibaldi and Ferrari, 1992; Lavenu et al., 1995; Fiorini and Tibaldi, 2012; Alvarado et al., 2016; Baize et al., 2020), and active strike-slip faults have been mapped both east and west of the Pisayambo fault (Champenois et al., 2017). Therefore, the slip rate measured across only the Pisayambo fault would not represent all the seismicity surrounding this structure.

The use of different magnitude-scaling relations could also change the MFDs produced by SHERIFS. For example, the length-based scaling relationships of Wesnousky (2008) for strike-slip faults intersects the one for Wells and Coppersmith (1994) at ∼100 km length, where both predict M ∼ 7.3. For shorter ruptures, Wesnousky (2008) predicts larger magnitudes than Wells and Coppersmith (1994) and vice versa for rupture lengths ≥100 km (in the model we use area-based magnitude-scaling relations but compare two length-based relationships here for consistency). Thus, using Wesnousky

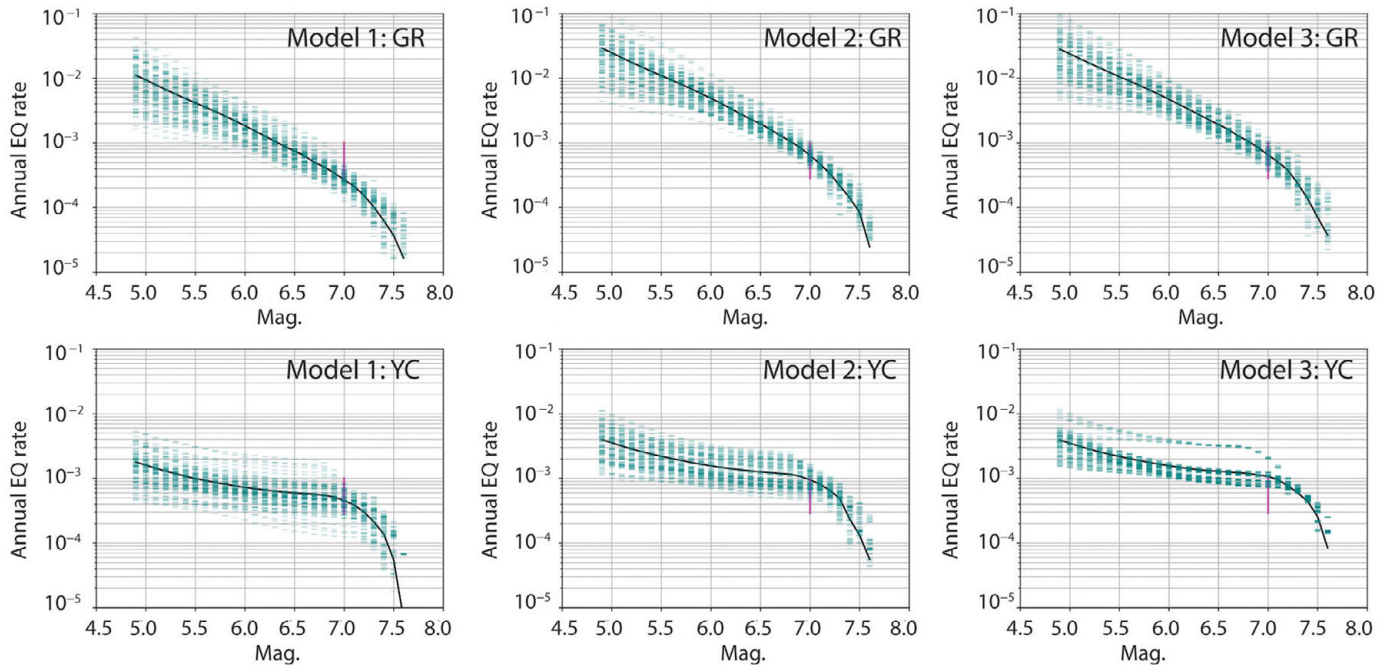**(a)** Cumulative MFDs: Set 1 (including the Pisayambo fault)
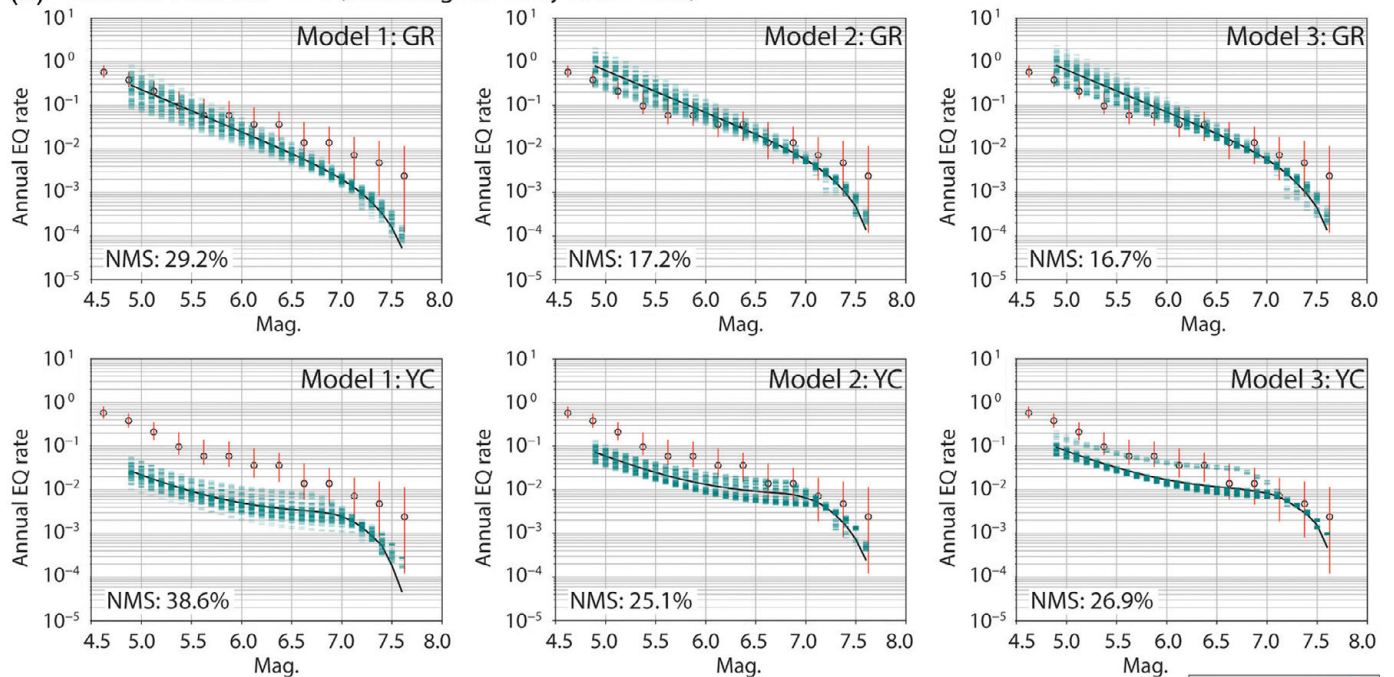
**(b)** Cumulative MFDs: Set 2 (excluding the Pisayambo fault)

Figure 6. Cumulative MFDs computed with SHERIFS for all models (a) with and (b) without the Pisayambo fault segments. The green bars show all results from all branches of the logic tree for each model, and the black line is the mean MFD. The black circles show the mean rates in the observed catalog, and red bars show the 95% confidence interval about the mean. All the computed models use either a Gutenber–Richter (GR) MFD or hybrid characteristic (Youngs and Coppersmith, 1985) MFD (YC) as predefined MFD shapes to follow. Slip rates for Model 1, 2, and 3 are defined in Figure 5. The color version of this figure is available only in the electronic edition.

(2008) would mean that the longest ruptures would produce lower magnitude earthquakes than Wells and Coppersmith (1994), reducing the value of M_{max}, and each using less of the seismic moment budget. Because the *b*-value is controlled by the modeler, the impact is likely to be of the same type as changing M_{max}, which we discuss below. Finally, because changing M_{max} does not alter our main results concerning slip-rate variation (Fig. 8), we interpret that using a different scaling relation would also not change this outcome.

(a) Participation rates for Rumipamba segment: Set 1 (including the Pisayambo fault)

(b) Participation rates for Rumipamba segment: Set 2 (excluding the Pisayambo fault)

SHERIFS rates
Mean SHERIFS rate
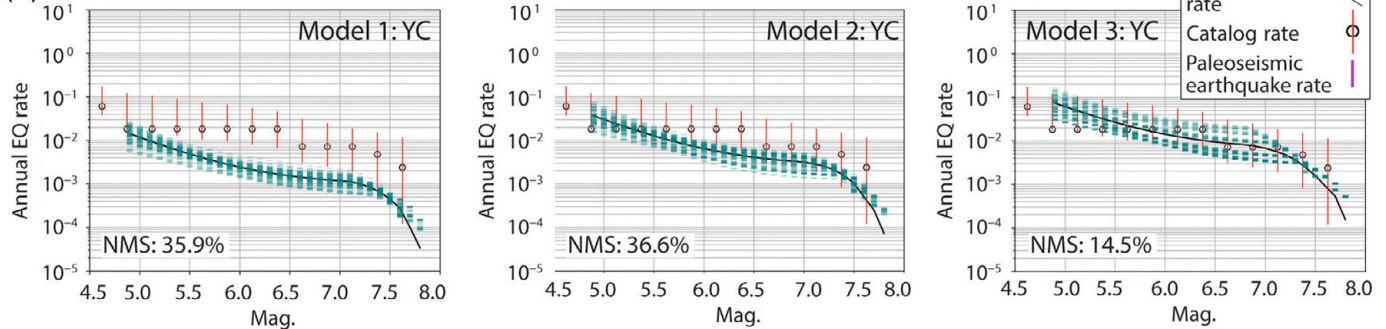Paleoseismic earthquake rate
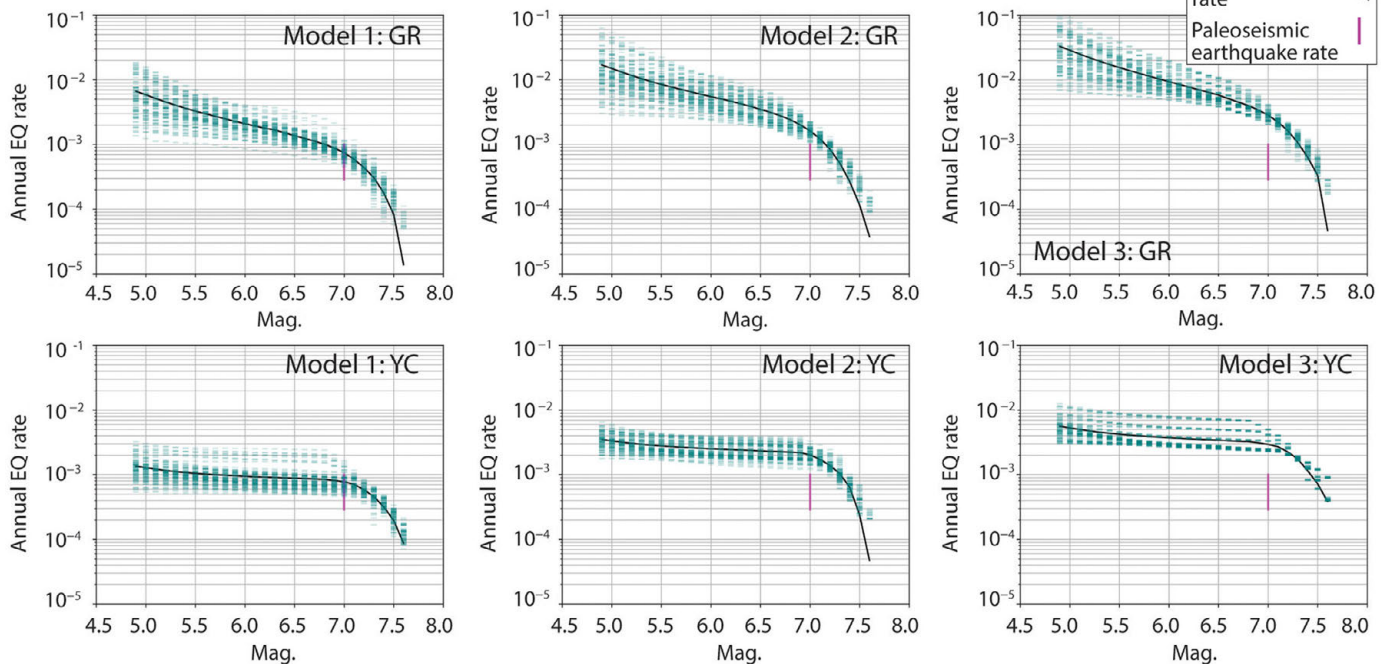
NMS values

In addition to producing MFDs that fit better with the catalog earthquake rates, the faster slip-rate models (Model 2 and 3) also result in relatively lower systemwide NMS ratios. These lower NMS ratios are likely the result of the moment budget allowing for more larger events, thereby increasing the rates of all earthquakes and using more of the moment budget without violating the shape of the MFD. There are geological processes that could account for NMS such as fault creep. High NMS

Figure 7. Computed cumulative earthquake participation rates for the Rumipamba segment of the PPF compared with paleoseismic earthquake rates from the Baize *et al.* (2015) paleoseismic trench. (a) Set 1 and (b) Set 2 use either a Gutenber–Richter (GR) MFD or hybrid characteristic MFD (YC) as predefined MFD shapes. Slip rates for Model 1, 2, and 3 are defined in Figure 5. The vertical purple bar indicates the paleoseismic rate of one M > 7.0 earthquake every 1000–3500 yr. The color version of this figure is available only in the electronic edition.

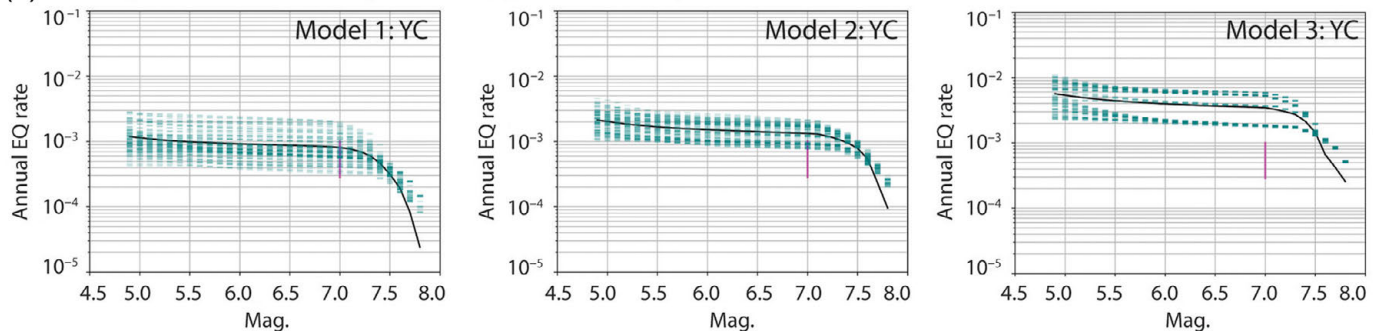**(a)** Cumulative MFDs: no Pisayambo fault, YC distribution, $M_{max} = 7.8$
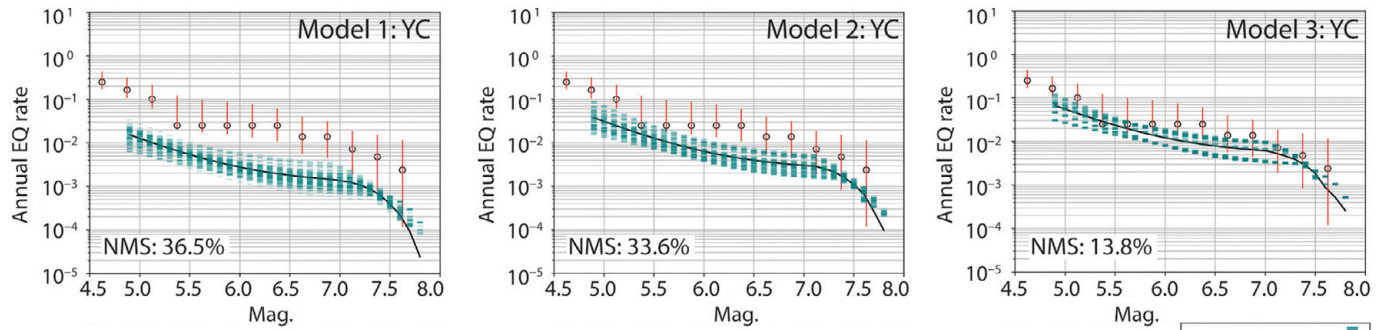
(b) Cumulative MFDs: no Pisayambo fault, YC distribution, $M_{max} = 7.8$, 5 km buffer catalog

(c) Participation rates for Rumipamba segment: no Pisayambo fault, YC distribution, $M_{max} = 7.8$

Figure 8. SHERIFS computed MFDs considering exclusion of the Pisayambo fault, $M_{max} = 7.8$, and a hybrid characteristic (YC) MFD as inputs. (a) Computed cumulative MFDs for Model 1–3 compared with the original catalog or (b) a 5 km buffer zone catalog. (c) Computed cumulative earthquake participation rates for the Rumipamba segment of the PPF compared with paleoseismic earthquake rates from the Baize *et al.* (2015) paleoseismic trench. Slip rates for Models 1, 2, and 3 are defined in Figure 5. The color version of this figure is available only in the electronic edition.

percentages >30%–40% could also result from the fault source model not accurately representing the observed seismicity, or conversely, that a large portion of the observed seismicity is not being produced by the fault (e.g., Chartier *et al.*, 2019). We interpret that the higher NMS percentages in Model 1 compared with Model 2 and 3 result from one or a few large earthquakes spending the entire moment-rate budget of a fault segment, and not allowing other, faster deforming neighboring segments to be involved in multisegment ruptures that utilize their remaining moment budgets. This interpretation suggests again that the moment budget resulting from the lower, Model 1 slip rates cannot account for all the fault system seismicity.

The models using a GR MFD shape have lower NMS percentages than their hybrid-characteristic (YC) counterparts (Fig. 6). This result is most likely due to the GR models allowing a larger proportion of moderate-size earthquakes to spend the slip rate in smaller increments, permitting the more frequent use of individual segment ruptures. However, because the moment budget is spent on a higher frequency

of moderate earthquakes, SHERIFS underestimates the larger earthquake frequencies resulting in a poorer fit of the GR models with the catalogs compared with the YC models (Fig. 6).

Paleoseismic earthquake rates
Paleoseismic earthquake rates on the Rumipamba segment (Baize *et al.*, 2015) are lower than the computed participation rates of the best-fitting SHERIFS models (Set 2, Model 2:YC

and Model 3:YC) while overlapping with all iterations of Model 1 and all models in Set 1 (Fig. 7). Despite this misfit, we still prefer Set 2, Model 2YC and Model 3:YC. The reason for this preference is the paleoseismic earthquake rate for M ≥ 7 is also lower than the observed catalog rate, and it may not accurately record all the large earthquakes that ruptured the Rumipamba segment of the PPF. The historical catalog places, albeit with significant uncertainty, the 1698 M 7.25 and 1645 M 7.0 epicenters along the Rumipamba segment, whereas the 1797 M 7.6 earthquake is located <30 km along strike to the north (Fig. 3; Beauval *et al.*, 2010). Given their epicenters and magnitudes, these three earthquakes would have likely ruptured the Rumipamba or parallel fault segments resulting in an earthquake rate of three M ≥ 7 earthquakes in the last 500 yr, significantly greater than the paleoseismic earthquake rate of one M ≥ 7 earthquake every 1000–3500 yr (Baize *et al.*, 2015). This discrepancy demonstrates that, if these historical earthquakes ruptured the PPF system, the paleoseismic trench does not record every earthquake along this portion of the PPF.

Missing earthquake events in a paleoseismic study are expected and could result from rupture propagation along a parallel fault segment, no surface rupture occurring, and/or low sedimentation rates. For example, paleoearthquake detection probability curves from the Uniform California Earthquake Forearcast (UCERF) 3 model (Weldon and Biasi, 2013) and the 2022 New Zealand National Seismic Hazard Model (Coffey *et al.*, 2022) indicate, even at the greatest rupture lengths, a probability of ~0.8 and ~0.45 (respectively) that an M 7 earthquake would be detectable in a paleoseismic study. In addition, paleoseismic trenching along the El Salvador fault zone, which was recently ruptured by a 2001 M 6.6 earthquake, shows that earthquakes of this magnitude and lower are difficult to observe in the stratigraphic record (Canora *et al.*, 2012). The authors of this study suggest that the earthquake recurrence interval from the paleoseismic record of this strike-slip forearc fault, similar in tectonic setting to the PPF, should be treated as the minimum. These observations further argue that slip rates and earthquake recurrence intervals observed in paleoseismic studies on a single fault segment should not be the sole input into fault source models.

Impact of M_{max}
Using M_{max} of 7.8 or 7.9 in the Set 2 YC models results in a better fit of the computed rates with the catalog rates for M > 7.0, and a better fit with the paleoearthquake data in the case of the long-term geomorphic model (Model 2) (Fig. 8, Fig. S2). However, because high-magnitude earthquakes utilize a large portion of the moment budget and leave less to be distributed among lower magnitudes, these models underestimate lower earthquakes rates. Therefore, we interpret that these results are not necessarily indicative of the correct M_{max} to use for the PPF, and several M_{max} values should be input as different branches of a logic tree in a PSHA model.

Although the computed M_{max} = 7.8 and 7.9 MFDs suggest that there is not enough moment budget to produce the largest earthquakes at the observed rates while maintaining the prescribed MFD shape, there are geologic scenarios that can explain this misfit. For example, we only use strike-slip rates as inputs on the PPF and assume that all the earthquakes are derived from this slip component. However, at the northern end of the PPF the Latacunga fold-and-thrust belt branches northward from the PPF system (Fig. 2; Tibaldi and Ferrari, 1992; Lavenu *et al.*, 1995; Fiorini and Tibaldi, 2012; Alvarado *et al.*, 2016; Baize *et al.*, 2020) and probably accommodates some of the convergence modeled by geodesy (Marinière *et al.*, 2020; Jarrin, 2021). Some of the observed seismicity (Fig. 3) could result from these structures, or other unmapped reverse faults, and therefore would not be modeled by our strike-slip rate-derived moment budget alone. For example, the 1868 M 7.2–7.3 Ambato earthquake could have occurred on a thrust fault splaying to the north away from the PPF. The same argument holds true for the southern end of the PPF, where extension in the Gulf of Guayaquil also results in seismicity on normal faults and resolvable divergence in the geodetic block model (Fig. 5; Dumont *et al.*, 2005; Witt *et al.*, 2006; Jarrin, 2021). Unfortunately the locations, geometries, and slip rates on the individual dip-slip structures are not well constrained, but further studies of these structures and incorporating them into our models may improve the fit with the observed seismicity.

Conclusions
Using SHERIFS to calculate earthquake rates using different slip rates for the PPF, we find that slip rates measured across the entire width of the fault zone, such as those based on geodesy or long-term geomorphic offsets, produce MFDs that compare more favorably with the observed catalog. This result cautions against using only slip rates measured across single discrete fault segments within a fault zone, because these often slower slip rates do not provide enough of a moment budget to account for fault zone seismicity. This conclusion also suggests that off-fault damage and slip on parallel fault segments are important to consider in fault source models. We also show that the MFDs computed using a YC (hybrid characteristic) MFD shape have a better fit with the observed catalog when the Pisayambo fault and associated seismic nest are removed (Set 2). In addition, the model results that best fit the observed catalog are not consistent with paleoseismic earthquake rates observed on the Rumipamba section of the PPF. However, because the paleoseismic record suggests that not all the M ≥ 7.0 ruptures along the Rumipamba are recorded at the paleoseismic study location, we conclude that this comparison is not robust. By increasing M_{max} in our best-fitting models from M 7.6 to 7.8 or M 7.9, we compute MFDs that slightly underestimate earthquake rates for all but the largest magnitude bins. However, the additional slip-rate budget required for the increased moment release could be

acquired from dip-slip rates on fault systems that connect with the PPF, which are unaccounted for in our models. Because of this possibility, logic tree branches exploring variation in M_{max} should be considered in a fault source model of the PPF.

Data and Resources

Declaration of Competing Interests

The authors acknowledge that there are no conflicts of interest recorded.

Acknowledgments

References

Aguilar, J., J.-L. Chatelain, B. Guillier, and H. Yepes (1996). The Pisayambo, Ecuador, seismicity nest: towards the birth of a volcano? in *Geodinámica Andina, Troisième symposium international sur la Géodynamique Andine*, Collection Colloques et Séminaires, Institut de Recherche pour le Développement, ORSTOM édition Paris, 126–129 (in French).

Alvarado, A., L. Audin, J.-M. Nocquet, E. Jaillard, P. Mothes, P. Jarrín, M. Segovia, F. Rolandone, and D. Cisneros (2016). Partitioning of oblique convergence in the northern Andes subduction zone: Migration history and the present-day boundary of the North Andean Sliver in Ecuador, *Tectonics* **35,** no. 5, 1048–1065.

Alvarado, A. A. C. (2012). Néotectonique et cinématique de la déformation continentale en Equateur, *Ph.D. Thesis*, Université de Grenoble (in French).

Antoine, S. L., Y. Klinger, A. Delorme, K. Wang, R. Bürgmann, and R. D. Gold (2021). Diffuse deformation and surface faulting distribution from submetric image correlation along the 2019 Ridgecrest, California, ruptures, *Bull. Seismol. Soc. Am.* **111,** no. 5, 2275–2302.

Baize, S., L. Audin, A. Alvarado, H. Jomard, M. Bablon, J. Champenois, P. Espin, P. Samaniego, X. Quidelleur, and J.-L. Le Pennec (2020). Active tectonics and earthquake geology along the Pallatanga fault, central Andes of Ecuador, *Front. Earth Sci.* **8,** 193.

Baize, S., L. Audin, T. Winter, A. Alvarado, L. P. Moreno, M. Taipe, P. Reyes, P. Kauffmann, and H. Yepes (2015). Paleoseismology and tectonic geomorphology of the Pallatanga fault (central Ecuador), a major structure of the South-American crust, *Geomorphology* **237,** 14–28.

Beauval, C., P.-Y. Bard, and L. Danciu (2020). The influence of source- and ground-motion model choices on probabilistic seismic hazard levels at 6 sites in France, *Bull. Earthq. Eng.* **18,** 4551–4580.

Beauval, C., J. Marinière, H. Yepes, L. Audin, J.-M. Nocquet, A. Alvarado, S. Baize, J. Aguilar, J.-C. Singaucho, and H. Jomard (2018). A new seismic hazard model for Ecuador, *Bull. Seismol. Soc. Am.* **108,** no. 3A, 1443–1464.

Beauval, C., H. Yepes, W. H. Bakun, J. Egred, A. Alvarado, and J.-C. Singaucho (2010). Locations and magnitudes of historical earthquakes in the Sierra of Ecuador (1587–1996), *Geophys. J. Int.* **181,** no. 3, 1613–1633.

Beauval, C., H. Yepes, P. Palacios, M. Segovia, A. Alvarado, Y. Font, J. Aguilar, L. Troncoso, and S. Vaca (2013). An earthquake catalog for seismic hazard assessment in Ecuador, *Bull. Seismol. Soc. Am.* **103,** no. 2A, 773–786.

Brune, J. N. (1968). Seismic moment, seismicity, and rate of slip along major fault zones, *J. Geophys. Res.* **73,** no. 2, 777–784.

Canora, C., P. Villamor, J. Martínez-Díaz, K. R. Berryman, J. A. Álvarez-Gómez, R. Capote, and W. Hernández (2012). Paleoseismic analysis of the San Vicente segment of the El Salvador fault zone, El Salvador, Central America, *Geol. Acta* **10,** no. 2, 103–123.

Champenois, J., S. Baize, M. Vallée, H. Jomard, A. Alvarado, P. Espin, G. Ekström, and L. Audin (2017). Evidences of surface rupture associated with a low-magnitude (M_w5.0) shallow earthquake in the Ecuadorian Andes, *J. Geophys. Res.* **122,** no. 10, 8446–8458.

Chartier, T., O. Scotti, and H. Lyon-Caen (2019). SHERIFS: Opensource code for computing earthquake rates in fault systems and constructing hazard models, *Seismol. Res. Lett.* **90,** no. 4, 1678–1688.

Chartier, T., O. Scotti, H. Lyon-Caen, and A. Boiselet (2017). Methodology for earthquake rupture rate estimates of fault networks: example for the western Corinth rift, Greece, *Nat. Hazards Earth Syst. Sci.* **17,** no. 10, 1857–1869.

Chartier, T., O. Scotti, H. Lyon-Caen, K. Richard-Dinger, J. H. Dieterich, and B. E. Shaw (2021). Modelling earthquake rates and associated uncertainties in the Marmara Region, Turkey, *Nat. Hazards Earth Syst. Sci.* **21,** no. 8, 2733–2751.

Coffey, G., C. Rollins, R. Van Dissen, D. Rhoades, K. Thingbaijam, K. Clark, M. Gerstenberger, N. Litchfield, and A. Nicol (2022). *New Zealand National Seismic Hazard Model 2022: Earthquake Recurrence Derivation from Paleoseismic Data and Probability of Detection, GNS Science Rept. 2022/32*, GNS Science, New Zealand, 57 pp.

Cornell, C. A. (1968). Engineering seismic risk analysis, *Bull. Seismol. Soc. Am.* **58,** no. 5, 1583–1606.

Costa, C., A. Alvarado, F. Audemard, L. Audin, C. Benavente, F. H. Bezerra, J. Cembrano, G. González, M. López, E. Minaya, *et al.*

(2020). Hazardous faults of South America; compilation and overview, *J. South Am. Earth Sci.* **104,** 102,837.

Das, S., and C. Scholz (1983). Why large earthquakes do not nucleate at shallow depths, *Nature* **305,** no. 5935, 621–623.

Dolan, J. F., and B. D. Haravitch (2014). How well do surface slip measurements track slip at depth in large strike-slip earthquakes? the importance of fault structural maturity in controlling on-fault slip versus off-fault surface deformation, *Earth Planet. Sci. Lett.* **388,** 38–47.

Dumont, J. F., E. Santana, and W. Vilema (2005a). Morphologic evidence of active motion of the Zambapala Fault, Gulf of Guayaquil (Ecuador), *Geomorphology* **65,** nos. 3/4, 223–239.

Dumont, J.-F., E. Santana, W. Vilema, K. Pedoja, M. Ordonez, M. Cruz, N. Jimenez, and I. Zambrano (2005b). Morphological and microtectonic analysis of quaternary deformation from Puná and Santa Clara islands, Gulf of Guayaquil, Ecuador (South America), *Tectonophysics* **399,** nos. 1/4, 331–350.

Egbue, O., and J. Kellogg (2010). Pleistocene to present North Andean "escape", *Tectonophysics* **489,** nos. 1/4, 248–257.

Egred, J. (2004). Terremoto de Riobamba del 4 Febrero de 1797, in *Investigaciones en Geociencias*, A. Alvarado, A. Garcia-Aristizabal, P. Mothes, and M. Segovia (Editors), IRD, IG, Corporacion Editora Nacional, Municipio del Distrito Metropolitano de Quito, Quito, Ecuador, 67–86 pp (in Spanish).

Egred, J. (2009). Catalogo de terremotos del Ecuador 1541–2009, Escuela Politecnica Nacional, Instituto Geofisico, Quito, Ecuador (in Spanish).

Elliott, J., R. Walters, and T. Wright (2016). The role of space-based observation in understanding and responding to active tectonics and earthquakes, *Nat. Commun.* **7,** no. 1, 13,844.

Fiorini, E., and A. Tibaldi (2012). Quaternary tectonics in the central Interandean Valley, Ecuador: Fault-propagation folds, transfer faults and the Cotopaxi Volcano, *Glob. Planet. Change* **90,** 87–103.

Gardner, J., and L. Knopoff (1974). Is the sequence of earthquakes in southern California, with aftershocks removed, Poissonian? *Bull. Seismol. Soc. Am.* **64,** no. 5, 1363–1367.

Gerstenberger, M. C., W. Marzocchi, T. Allen, M. Pagani, J. Adams, L. Danciu, E. H. Field, H. Fujiwara, N. Luco, K.-F. Ma, *et al.* (2020). Probabilistic seismic hazard analysis at regional and national scales: State of the art and future challenges, *Rev. Geophys.* **58,** no. 2, e2019RG000653, doi: 10.1029/2019RG000653.

Gold, R. D., N. G. Reitman, R. W. Briggs, W. D. Barnhart, G. P. Hayes, and E. Wilson (2015). On-and off-fault deformation associated with the September 2013 M_w 7.7 Balochistan earthquake: Implications for geologic slip rate measurements, *Tectonophysics* **660,** 65–78.

Gutenberg, B., and C. Richter (1954). *Seismicity of the Earth and Associated Phenomena*. Princeton University Press, Princeton, New Jersey, U.S.A.

Hamling, I. J., S. Hreinsdóttir, K. Clark, J. Elliott, C. Liang, E. Fielding, N. Litchfield, P. Villamor, L. Wallace, T. J. Wright, *et al.* (2017). Complex multifault rupture during the 2016 M_w 7.8 Kaikōura earthquake, New Zealand, *Science* **356,** no. 6334, eaam7194, doi: 10.1126/science.aam7194.

Hanks, T. C., and W. H. Bakun (2008). M-logA observations for recent large earthquakes, *Bull. Seismol. Soc. Am.* **98,** no. 1, 490–494.

Jarrin, P. (2021). Cinématique actuelle dans les Andes du Nord par GPS, *Ph.D. Thesis*, Sorbonne Université.

Jarrin, P., J.-M. Nocquet, F. Rolandone, H. Mora-Páez, P. Mothes, and D. Cisneros (2023). Current motion and deformation of the Nazca Plate: New constraints from GPS measurements, *Geophys. J. Int.* **232,** no. 2, 842–863.

Lavenu, A., T. Winter, and F. Dávila (1995). A Pliocene–Quaternary compressional basin in the inter-Andean depression, central Ecuador, *Geophys. J. Int.* **121,** no. 1, 279–300.

Makropoulos, K. C., and P. W. Burton (1983). Seismic risk of circum-Pacific earthquakes I. Strain energy release, *Pure Appl. Geophys.* **121,** 247–267.

Marinière, J., J. Nocquet, C. Beauval, J. Champenois, L. Audin, A. Alvarado, S. Baize, and A. Socquet (2020). Geodetic evidence for shallow creep along the Quito fault, Ecuador, *Geophys. J. Int.* **220,** no. 3, 2039–2055.

McGuire, R. K. (2008). Probabilistic seismic hazard analysis: Early history, *Earthq. Eng. Struct. Dynam.* **37,** no. 3, 329–338.

McNulty, B. A. (1995). Pseudotachylyte generated in the semi-brittle and brittle regimes, Bench Canyon shear zone, central Sierra Nevada, *J. Struct. Geol.* **17,** no. 11, 1507–1521.

Meissner, R., and J. Strehlau (1982). Limits of stresses in continental crusts and their relation to the depth-frequency distribution of shallow earthquakes, *Tectonics* **1,** no. 1, 73–89.

Milliner, C., J. Dolan, J. Hollingsworth, S. Leprince, and F. Ayoub (2016). Comparison of coseismic near-field and off-fault surface deformation patterns of the 1992 M_w 7.3 Landers and 1999 M_w 7.1 Hector Mine earthquakes: Implications for controls on the distribution of surface strain, *Geophys. Res. Lett.* **43,** no. 19, 10–115.

Milliner, C. W., J. F. Dolan, J. Hollingsworth, S. Leprince, F. Ayoub, and C. G. Sammis (2015). Quantifying near-field and off-fault deformation patterns of the 1992 M_w 7.3 Landers earthquake, *Geochem. Geophys. Geosys.* **16,** no. 5, 1577–1598.

Mora-Páez, H., J. N. Kellogg, J. T. Freymueller, D. Mencin, R. M. Fernandes, H. Diederix, P. LaFemina, L. Cardona-Piedrahita, S. Lizarazo, J.-R. Peláez-Gaviria, *et al.* (2019). Crustal deformation in the northern Andes–A new GPS velocity field, *J. South Am. Earth Sci.* **89,** 76–91.

Nocquet, J.-M., J. C. Villegas-Lanza, M. Chlieh, P. Mothes, F. Rolandone, P. Jarrin, D. Cisneros, A. Alvarado, L. Audin, F. Bondoux, *et al.* (2014). Motion of continental slivers and creeping subduction in the northern Andes, *Nature Geosci.* **7,** no. 4, 287–291.

Ojo, A. O., H. Kao, Y. Jiang, M. Craymer, and J. Henton (2021). Strain accumulation and release rate in Canada: Implications for long-term crustal deformation and earthquake hazards, *J. Geophys. Res.* **126,** no. 4, e2020JB020529, doi: 10.1029/2020JB020529.

Oskin, M., L. Perg, D. Blumentritt, S. Mukhopadhyay, and A. Iriondo (2007). Slip rate of the Calico fault: Implications for geologic versus geodetic rate discrepancy in the eastern California shear zone, *J. Geophys. Res.* **112,** no. B3, doi: 10.1029/2006JB004451.

Pagani, M., I. D. Monell, G. Weatherill, L. Danciu, H. Crowley, V. Silva, P. Henshaw, L. Butler, M. Nastasi, L. Panzeri, *et al.* (2014). OpenQuake engine: An open hazard (and risk) software for the global earthquake model, *Seismol. Res. Lett.* **85,** no. 3, 692–702.

Papanikolaou, I. D., G. P. Roberts, and A. M. Michetti (2005). Fault scarps and deformation rates in Lazio–Abruzzo, central Italy: Comparison between geological fault slip-rate and GPS data, *Tectonophysics* **408,** nos. 1/4, 147–176.

Parra, H., M. Benito, and J. Gaspar-Escribano (2016). Seismic hazard assessment in continental Ecuador, *Bull. Earthq. Eng.* **14,** no. 8, 2129–2159.

Reasenberg, P. (1985). Second-order moment of central California seismicity, 1969–1982, *J. Geophys. Res.* **90,** no. B7, 5479–5495.

Rockwell, T. K., S. Lindvall, T. Dawson, R. Langridge, W. Lettis, and Y. Klinger (2002). Lateral offsets on surveyed cultural features resulting from the 1999 Izmit and Duzce earthquakes, Turkey, *Bull. Seismol. Soc. Am.* **92,** no. 1, 79–94.

Rodriguez Padilla, A. M., M. A. Quintana, R. M. Prado, B. J. Aguilar, T. A. Shea, M. E. Oskin, and L. Garcia (2022). Near-field high-resolution maps of the Ridgecrest earthquakes from aerial imagery, *Seismol. Res. Lett.* **93,** no. 1, 494–499.

Sibson, R. H. (1982). Fault zone models, heat flow, and the depth distribution of earthquakes in the continental crust of the United States, *Bull. Seismol. Soc. Am.* **72,** no. 1, 151–163.

Stirling, M., T. Goded, K. Berryman, and N. Litchfield (2013). Selection of earthquake scaling relationships for seismic-hazard analysis, *Bull. Seismol. Soc. Am.* **103,** no. 6, 2993–3011.

Styron, R. (2019). The impact of earthquake cycle variability on neotectonic and paleoseismic slip rate estimates, *Solid Earth* **10,** no. 1, 15–25.

Tibaldi, A., and L. Ferrari (1992). Latest pleistocene-holocene tectonics of the Ecuadorian Andes, *Tectonophysics* **205,** nos. 1/3, 109–125.

Vaca, S., M. Vallée, J.-M. Nocquet, and A. Alvarado (2019). Active deformation in Ecuador enlightened by a new waveform-based catalog of earthquake focal mechanisms, *J. South Am. Earth Sci.* **93,** 449–461.

Villegas-Lanza, J. C., M. Chlieh, O. Cavalié, H. Tavera, P. Baby, J. Chire-Chira, and J.-M. Nocquet (2016). Active tectonics of Peru: Heterogeneous interseismic coupling along the Nazca megathrust, rigid motion of the Peruvian Sliver, and Subandean shortening accommodation, *J. Geophys. Res.* **121,** no. 10, 7371–7394.

Visage, S., P. Souloumiac, N. Cubas, B. Maillot, S. Antoine, A. Delorme, and Y. Klinger (2023). Evolution of off-fault deformation of strike-slip fault in a sand-box experiment, *Tectonophysics* **847,** 229,704.

Ward, S. N. (1998). On the consistency of earthquake moment rates, geological fault data, and space geodetic strain: The United States, *Geophys. J. Int.* **134,** no. 1, 172–186.

Weichert, D. H. (1980). Estimation of the earthquake recurrence parameters for unequal observation periods for different magnitudes, *Bull. Seismol. Soc. Am.* **70,** no. 4, 1337–1346.

Weldon, R. J., and G. P. Biasi (2013). Appendix I: Probability of detection of ground rupture at paleoseismic sites, *U.S. Geol. Surv. Open-File Rept. 2013-1165-I and California Geol. Surv. Special Rept. 228-I,* available at https://pubs.usgs.gov/of/2013/1165/pdf/ofr2013-1165_appendixI.pdf (last accessed October 2023).

Wells, D. L., and K. J. Coppersmith (1994). New empirical relationships among magnitude, rupture length, rupture width, rupture area, and surface displacement, *Bull. Seismol. Soc. Am.* **84,** no. 4, 974–1002.

Wesnousky, S. G. (2008). Displacement and geometrical characteristics of earthquake surface ruptures: Issues and implications for seismic-hazard analysis and the process of earthquake rupture, *Bull. Seismol. Soc. Am.* **98,** no. 4, 1609–1632.

Williams, J. N., D. J. Barrell, M. W. Stirling, K. M. Sauer, G. C. Duke, and K. X. Hao (2018). Surface rupture of the Hundalee fault during the 2016 M_w 7.8 Kaikōura earthquake, *Bull. Seismol. Soc. Am.* **108,** no. 3B, 1540–1555.

Winter, T., J.-P. Avouac, and A. Lavenu (1993). Late Quaternary kinematics of the Pallatanga strike-slip fault (central Ecuador) from topographic measurements of displaced morphological features, *Geophys. J. Int.* **115,** no. 3, 905–920.

Witt, C., J. Bourgois, F. Michaud, M. Ordoñez, N. Jiménez, and M. Sosson (2006). Development of the Gulf of Guayaquil (Ecuador) during the Quaternary as an effect of the North Andean block tectonic escape, *Tectonics* **25,** no. 3, doi: 10.1029/2004TC001723.

Wu, S.-C., C. A. Cornell, and S. R. Winterstein (1995). A hybrid recurrence model and its implication on seismic hazard results, *Bull. Seismol. Soc. Am.* **85,** no. 1, 1–16.

Yepes, H., L. Audin, A. Alvarado, C. Beauval, J. Aguilar, Y. Font, and F. Cotton (2016). A new view for the geodynamics of Ecuador: Implication in seismogenic source definition and seismic hazard assessment, *Tectonics* **35,** no. 5, 1249–1279.

Youngs, R. R., and K. J. Coppersmith (1985). Implications of fault slip rates and earthquake recurrence models to probabilistic seismic hazard estimates, *Bull. Seismol. Soc. Am.* **75,** no. 4, 939–964.

Zinke, R., J. Hollingsworth, and J. F. Dolan (2014). Surface slip and off-fault deformation patterns in the 2013 M_w 7.7 Balochistan, Pakistan earthquake: Implications for controls on the distribution of near-surface coseismic slip, *Geochem. Geophys. Geosys.* **15,** no. 12, 5034–5050.